ARMY RESEARCH LABORATORY

The Development of a Super-α_2 Titanium Aluminide Alloy Consolidated by Rapid Omnidirectional Compaction

Wego Wang and Martin G. H. Wells

ARL-TR-341

March 1994

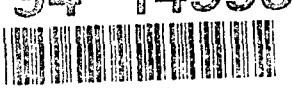

The findings in this report are not to be construed as an official Department of the Army position unless so designated by other authorized documents.

Citation of manufacturer's or trade names does not constitute an official endorsement or approval of the use thereof.

Destroy this report when it is no longer needed. Do not return it to the originator.

REPORT DOCUMENTATION PAGE

Form Approved
OMB No. 0704-0188

1. AGENCY USE ONLY (Leave blank)	2. REPORT DATE	3. REPORT TYPE AND DATES COVERED
	March 1994	Final Report

4. TITLE AND SUBTITLE
The Development of a Super-α_2 Titanium Aluminide Alloy Consolidated by Rapid Omnidirectional Compaction

5. FUNDING NUMBERS

6. AUTHOR(S)
Wego Wang and Martin G. H. Wells

7. PERFORMING ORGANIZATION NAME(S) AND ADDRESS(ES)
U.S. Army Research Laboratory
Watertown, MA 02172-0001
ATTN: AMSRL-MA-CC

8. PERFORMING ORGANIZATION REPORT NUMBER
ARL-TR-341

9. SPONSORING/MONITORING AGENCY NAME(S) AND ADDRESS(ES)
U.S. Army Research Laboratory
2800 Powder Mill Road
Adelphi, MD 20783-1197

10. SPONSORING/MONITORING AGENCY REPORT NUMBER

11. SUPPLEMENTARY NOTES

12a. DISTRIBUTION/AVAILABILITY STATEMENT
Approved for public release; distribution unlimited.

12b. DISTRIBUTION CODE

13. ABSTRACT (Maximum 200 words)

Six super-α_2 titanium aluminide "pancakes" were produced by rapid omnidirectional compaction of prealloyed Ti-25Al-10Nb-3V-1Mo (at%) powder. The β-transus temperature was found to be about 1,090°C (1,990°F). The alloy was heat-treated with four different schedules to develop various structure combinations of α_2 and β, and followed by a series of microstructural analyses and mechanical property determinations. The highest ultimate tensile and yield strengths attained at room temperatures were 1,174.9 and 977.7 MPa (170.4 and 141.8 ksi), respectively. However, the elongation was less than 2%. The alloy also showed good stress rupture resistance. It was observed that, under otherwise similar conditions, ductility increased with the aspect ratio of the α_2 phase but the tensile strength is inversely related to the aspect ratio. During the tensile and stress rupture tests, multiple transverse cracks nucleated in the longitudinal direction on the specimen surface and within the specimen simultaneously. Cracks nucleated randomly throughout the fine α_2 /β matrix, coarse primary α_2 phase, or the boundaries between the α_2 /β matrix and primary α_2. No preferential crack nucleation sites could be found. The coalescence of cracks at the same horizontal plane (transverse to the applied stress) was the fracture-controlling factor. Colony-type intergranular fracture with ductile microvoids was predominant in the stress-ruptured surface, however either colony-type intergranular or sheared transgranular fracture dominated the tensile fracture depending on the grain morphology. Compared with a similar hot isostatically pressed material, the current alloy showed superior mechanical properties due to a finer microstructure.

14. SUBJECT TERMS	15. NUMBER OF PAGES
Titanium aluminide, Rapid omnidirectional compaction, Fracture mechanism	45
	16. PRICE CODE

17. SECURITY CLASSIFICATION OF REPORT	18. SECURITY CLASSIFICATION OF THIS PAGE	19. SECURITY CLASSIFICATION OF ABSTRACT	20. LIMITATION OF ABSTRACT
Unclassified	Unclassified	Unclassified	UL

CONTENTS

FIGURES

Page

Page

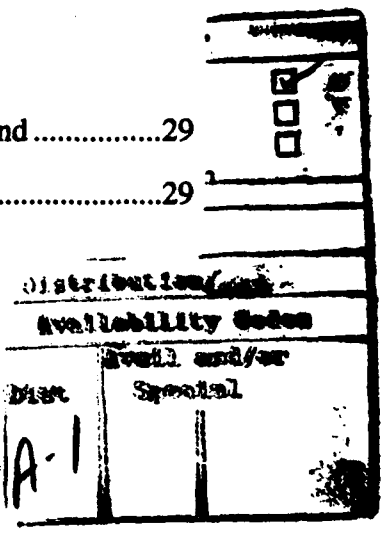

Page

TABLES

Page

INTRODUCTION

The integrated high performance turbine engine technology (IHPTET) and national aerospace plane (NASP) programs exemplify the need for new high temperature materials, and their success depends, to a large extent, on the development of new materials and processing technology [1-3]. The low density, high modulus, and persistent high temperature strength of titanium aluminide alloys make them attractive candidates for applications at high temperatures in advanced gas turbine engines. However, poor room temperature ductility dramatically restricts their otherwise great potential [4,5]. The addition of Nb stabilizes the bcc β phase and suppresses the bcc to hcp martensitic transformation [6], and subsequently improves the ambient temperature ductility [7]. The development of the super–α_2 titanium aluminide alloy promises a new engineering material for the aerospace industry. Studies on microstructure [8], processing [9], fatigue crack growth behavior [10], fracture and toughness mechanism [11, 12], weldability [13] and hot deformation characteristics [14] of this alloy have been reported. The current study is focused on the structure and properties of super-α_2 titanium aluminide consolidated by rapid omnidirectional compaction (ROC) using prealloyed powder.

MATERIALS AND PROCESSES

Materials

The material used for this study is a titanium aluminide alloy, Ti-25Al-10Nb-3V-1Mo (at%) [Ti-14.1Al-19.5Nb-3.2V-2Mo (wt%)]. The binary Ti-Al [15] and the pseudo-binary Ti_3Al-Nb [16] phase diagram are shown in Figures 1 and 2. α_2, an ordered hexagonal phase based on Ti_3Al, has a DO_{19} structure as shown in Figure 3 [17].

The initial prealloyed electrode was prepared by induction skull melting at the Durion Co., Dayton, OH. The powder was atomized by the plasma rotating electrode process (PREP) at Nuclear Metals, Inc., Concord, MA. In the process, a helium plasma is used to melt the end of a spinning electrode bar. Molten metal droplets are spun off and solidify in flight in the helium atmosphere. The PREP powder features a spherical shape with low oxygen content compared with other atomization processes. Subsequently, the powder was consolidated at Ladish Corp. into six pancakes by ROC at 1,052°C (1,295°F) for 15 seconds at a 60 tsi (827.4 MPa/120 ksi) pressure. The dimensions of the pancakes are 16.5 cm (6.5 in) in diameter by 7.0 cm (2.75 in) thick with a weight of approximately 7.7 kg (17 lb). The relatively low thermal exposure given the powder during ROC processing results in retention of a very fine microstructure inherent from PREP powder and the development of excellent mechanical properties [18]. The average measured density of these six pancakes is 4.735 g/cc (0.170 lb/in^3) [19]. The detailed density data along with other information regarding each individual pancake are listed in Table 1. The chemical analysis of the material at various process stages is summarized in Table 2.

Rapid Omnidirectional Compaction

Cost is always a concern for the manufacturing industry. Powder metallurgy provides a low cost process for mass production. ROC is a powder metallurgy consolidation process which is particularly effective for rapidly solidified hard intermetallic alloys with inherent fine microstructure. Processing steps of a typical ROC are shown in Figure 4 [18]. First, the fluid die components are forged and machined for cast; after die assembling, the cavity is filled with powder and the die sealed. The whole fluid die assembly containing the powder is preheated and then consolidated in a forge press. The powder is omnidirectionally compacted during this process, the externally applied force from a uniaxial ram crates a hydrostatic pressure which typically ranges

Figure. 1. Binary Ti-Al phase diagram [15].

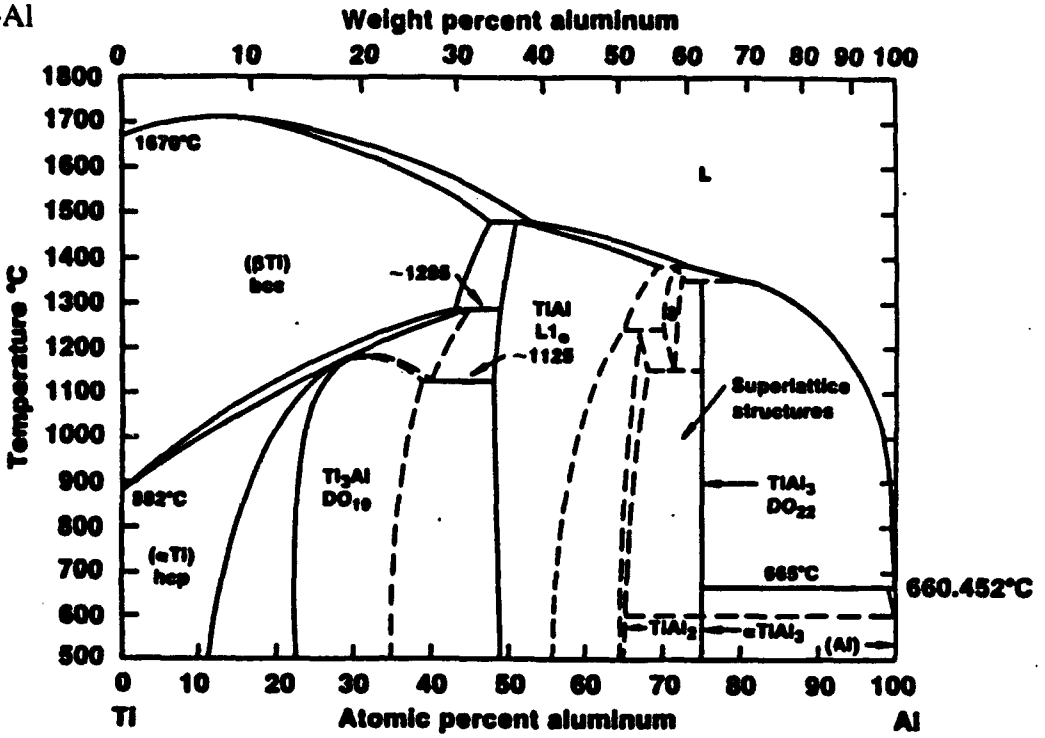

Figure. 2. Pseudo-binary Ti_3Al-Nb phase diagram [16].

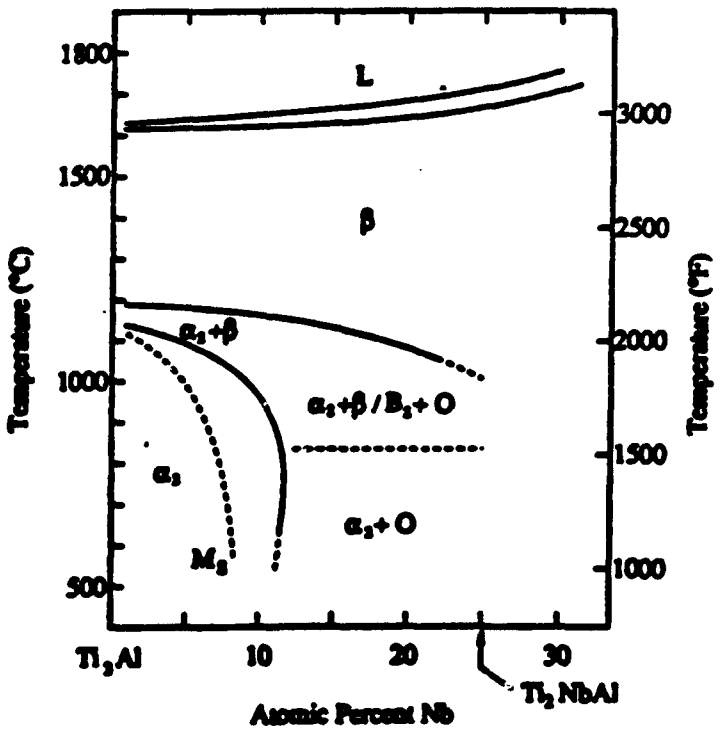

Figure. 3. The HCP DO_{19} structure of Ti_3Al intermetallic compound [17].

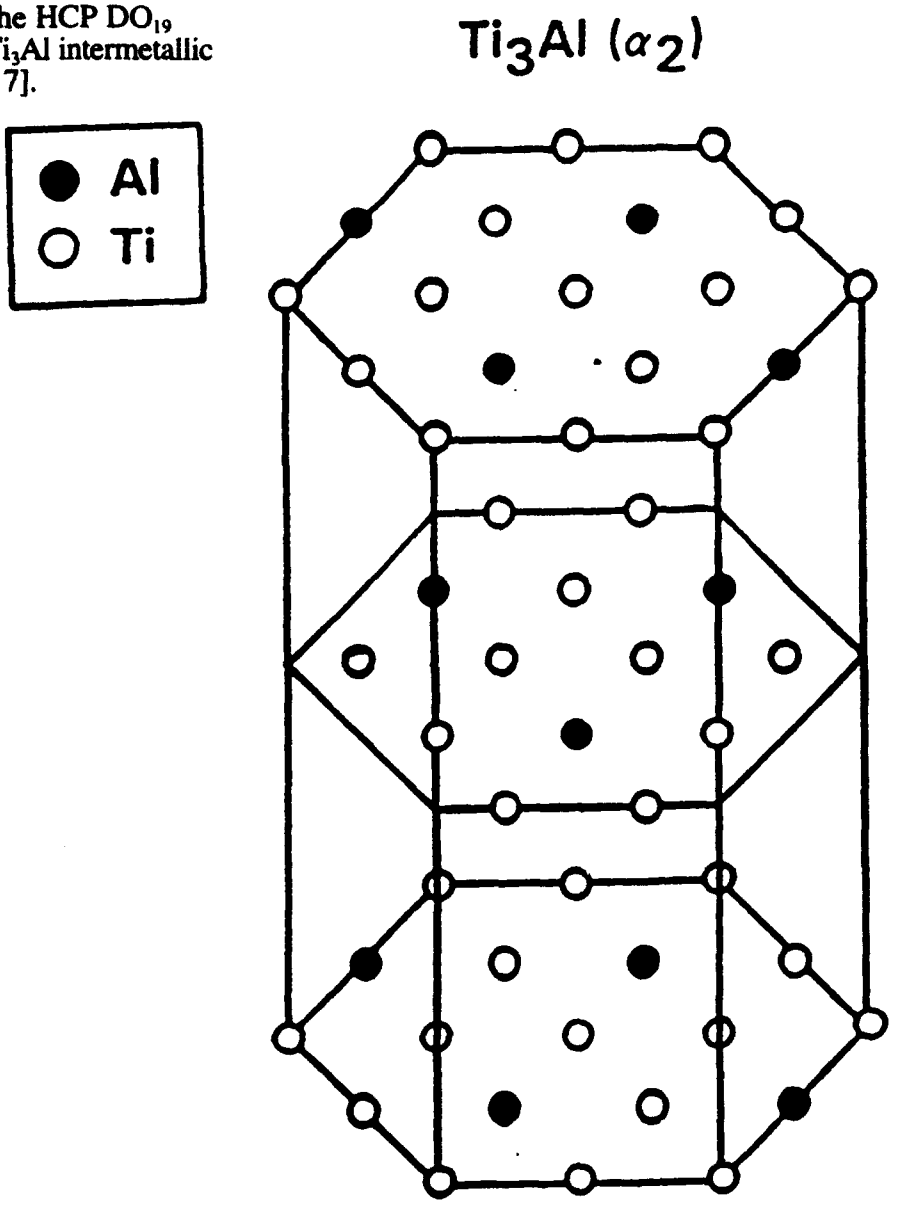

Table 1. Density [19]

Pancake	Measured Density g/cc (lb/in^3)	Powder Source	Impurity (ppm)		
			O	N	Fe
1 (APQ-2)	4.735 (0.170)	PREP -35*	850	57	NA
2 (APQ-3)	4.735 (0.170)	NA	NA	NA	NA
3 (APQ-4)	4.736 (0.170)	NA	NA	NA	NA
4 (APQ-5)	4.739 (0.171)	NA	NA	NA	NA
5 (APQ-6)	4.735 (0.170)	PREP -35	880	63	NA
6 (APQ-7)	4.732 (0.170)	PREP -35	850	70	580
Average	4.735 (0.170)	NA	NA	NA	NA

* less than 35 mesh

Table 2. Chemical analysis of the material at various stages [19]

Material Form	Element (wt%)					
	Al	Nb	V	Mo	O	Fe
Aim	14.1	19.5	3.2	2	-	0
Electrode	13.4	18.8	3.01	1.81	0.072	0.046
Powder	12.8	19.2	3.10	1.91	0.082	0.069
Pancake	NA	NA	NA	NA	0.086	NA

from 345 to 890 MPa (50 to 130 ksi). The fluid die is removed after consolidation by chemical and/or mechanical methods. The finished parts are usually fully dense with a fine-grained microstructure. For some powders, preheat temperatures are about the same as for hot isostatic pressing, but other materials can be ROC'ed at temperatures that are several hundred degrees Fahrenheit cooler than hot isostatic pressing temperatures. Thermally sensitive materials such as rapidly solidified powders can still retain their metastable microstructures with resultant property benefits due to the shorter exposure at a lower temperatures for the ROC process. In addition to a fine-grained structure and the excellent dimensional control, the ROC process can also have relatively lower production costs, typically 50% of those of hot isostatic pressing, provided an in-place forging press is available.

The microstructure of as-ROC'ed pancake samples pressed as above show a mixture of α_2 + β phases. As shown in Figure 5, the primary α_2 grains are spread throughout the β matrix in which some acicular α_2 has also been precipitated.

Heat Treatment

A series of heat treatments was conducted on slices cut from the pancakes. Image analysis of α_2 phase was used to determine the β transus temperature. The results are summarized in Table 3. We conclude that the β transus temperature is about 1,090°C (1,990°F).

Selected macrographs are shown in Figures 6-9. In Figures 6 and 7, for a sample heat treated at 1,093°C (2,000°F) for one hour, only a very limited amount of α_2 phase is scattered throughout the β matrix. The distribution of α_2 phase is not uniform and suggested some segregation along grain boundaries. This agglomeration of α_2 phase is due to the grain boundary "pipe diffusion" effect of oxygen, an alpha stabilizer. A clear edge (surface) effect can also be

Figure. 4. Steps of a typical rapid omnidirectional compaction process [18].

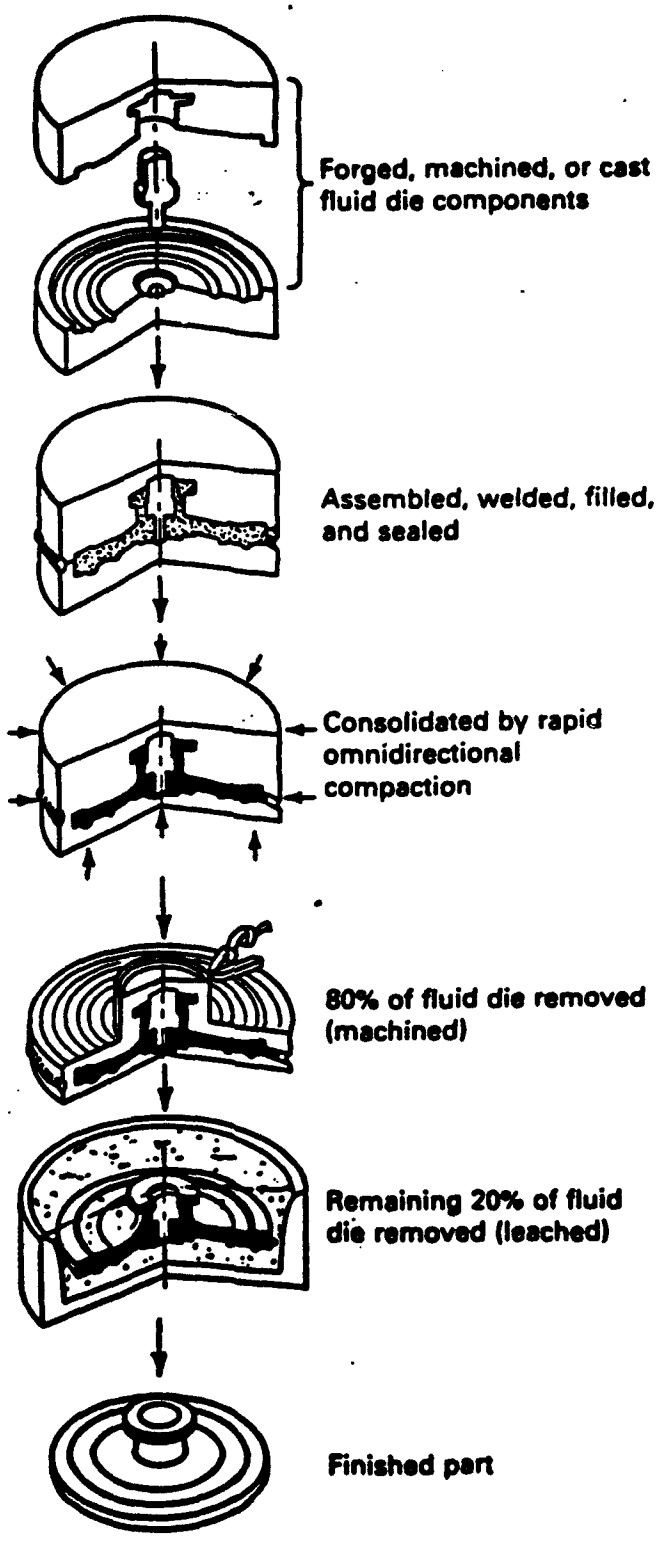

Figure. 5. Microstructure of as-ROC'ed material.

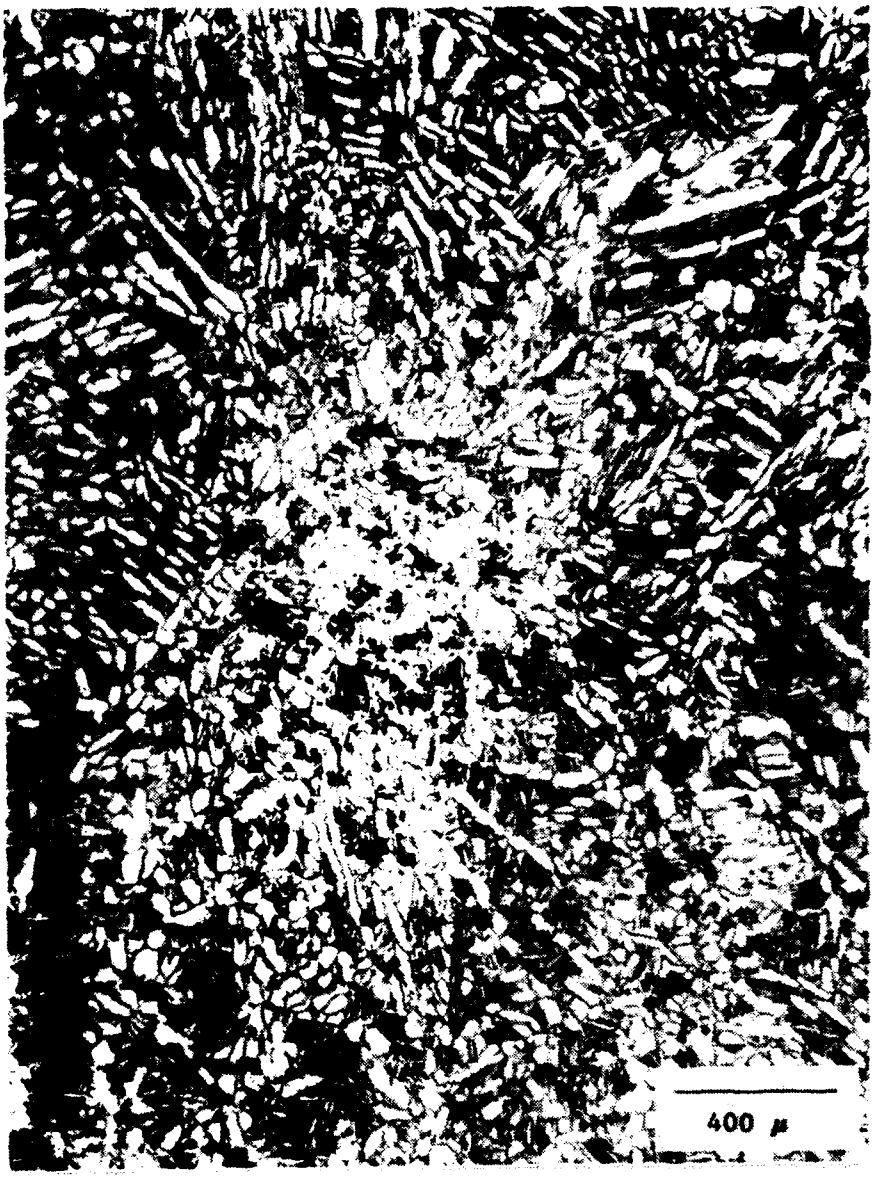

Figure. 6. Microstructure of a sample heat treated at 1,093°C (2,000°F) for one hour; scattered α_2 phase is found throughout the matrix.

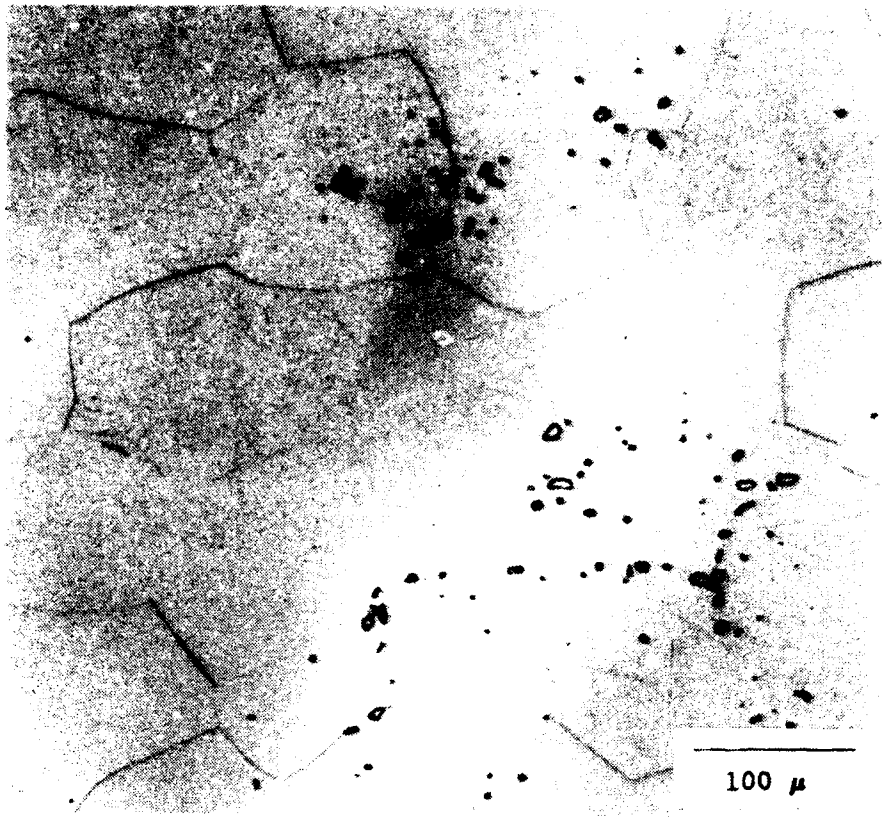

Figure. 7. Edge effects observed in a sample heat treated at 1,093°C (2,000°F) for one hour.

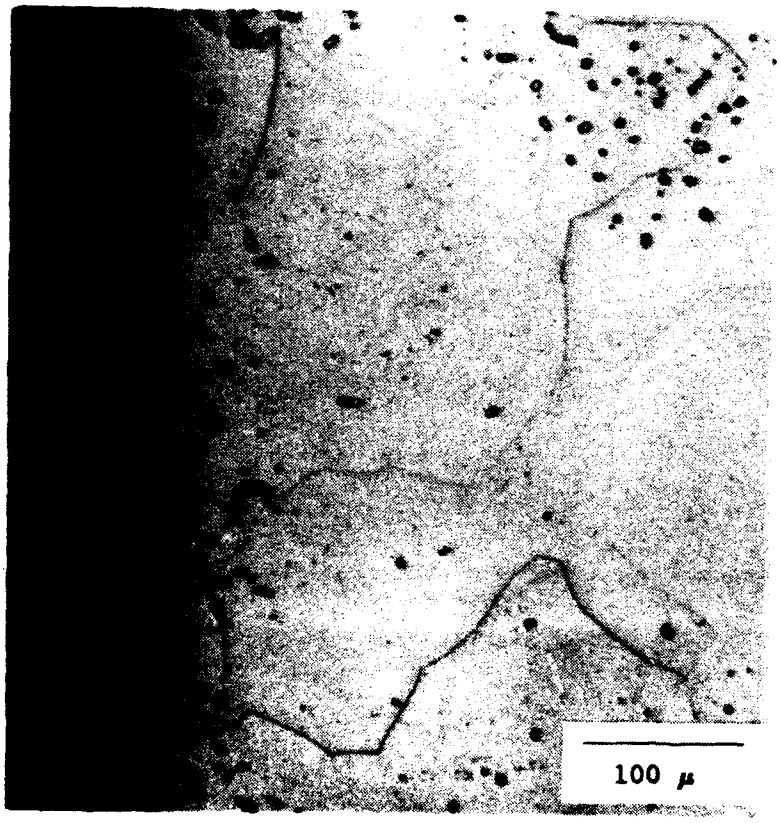

Figure. 8. Microstructure of a sample heat treated below the β-transus temperature at 1,071°C (1,960°F) for one hour, a large amount of primary α_2 phase is observed.

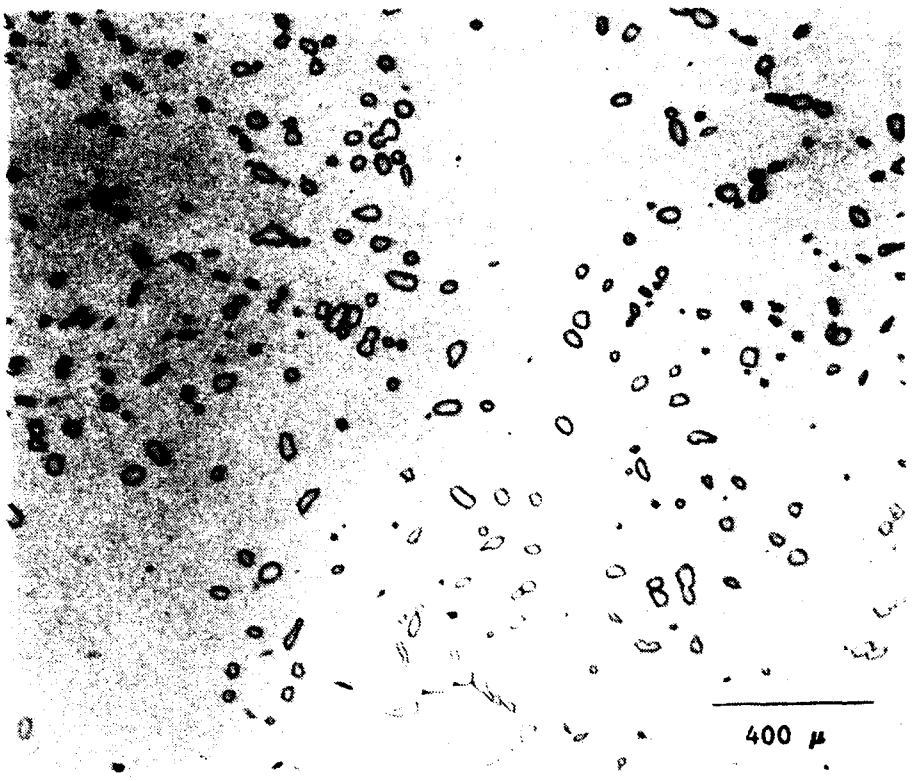

Figure. 9. Profound edge effect found in a sample heat treated at 1,071°C (1,960°F) for one hour.

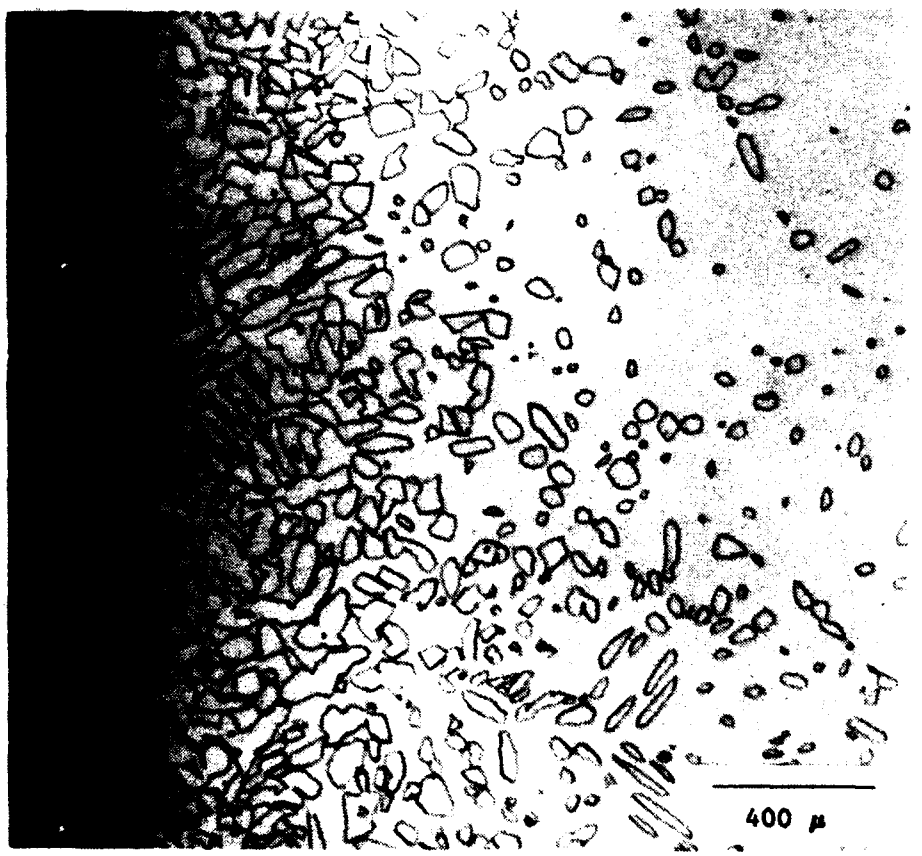

observed. A sample heat treated below the β transus temperature at 1,071°C (1,960°F) for one hour exhibited a large amount of primary α_2 phase in the matrix. A profound edge effect was also observed, as shown by comparing Figures 8 and 9.

Table 3. Results of image analysis of α_2 phase

Solution Temperature °C (°F)	Time (Hour)	Relative Volume of α_2 Phase	
		%	Standard Deviation
1,093 (2,000)	1	1.0	1.4
1,084 (1,984)	1	5.5	4.2
1,071 (1,960)	1	7.3	4.0
1,071 (1,960)	8.5	11.7	5.2
1,039 (1,902)	1	43.4	5.8

Profound effects of alloy composition and morphologies of the constituent phases on mechanical properties are expected. The best ductility is usually found with samples that are β-stabilized, air cooled then aged at an intermediate temperature. The plate-like α_2 usually ensures a better ductility, while an equiaxed α_2 structure is associated with lower ductilities. The best creep behavior can also be expected from samples that are β heat treated then followed by intermediate cooling. The heat treatment schedules listed in Table 4 and plotted in Figure 10 were followed to find the microstructure which optimized the mechanical properties. Also given in Table 4 is the resultant aspect ratio (the ratio between the length and the width) of the transformed α_2 phase (except the as-ROC'ed material where the aspect ratio refers to the primary α_2). The first heat treatment cycle started with an exposure above the β-transus followed by a water quench and a double aging treatment. The second involved a solution treatment below the β–transus with a direct quench to a lower aging temperature. The third sequence involved a cycling above and below the β-transus, and the fourth treatment was a high-above β-transus solution treatment with a direct quench to a lower temperature aging.

Microstructural analysis of the heat treated specimens revealed very different microstructures as shown in Figures 11-14. Heat treatment 1 (Figure 11) produced scattered areas of primary α_2 in a mixed α_2/β matrix with well defined β grains. Heat treatment 2 (Figure 12) gave large amounts of equiaxed primary α_2 along with fine acicular α_2 in a β matrix. No β grains could be detected because the solution temperature was below the β-transus temperature. Heat treatment 3, cycled above and below the β-transus temperature, resulted in a transformed colony-type α_2 structure with grain-boundary α_2 present as exhibited in Figures 13(a) and (b). Heat treatment 4 resulted in a fine Widmanstatten appearance as shown in Figure 14. No porosity was observed in the as-ROC'ed sample or any of the heat-treated samples. A notable difference was observed between samples heat treated by schedules 2 and 4 (Figures 12 and 14). Coarse equiaxed primary α_2 with no β grains was observed for schedule 2 in contrast to clearly defined β grains containing fine acicular α_2 for schedule 4. α_2 has completely transformed to the β phase by heat treatments 3 and 4 and left little or no primary α_2 phase in the matrix.

MECHANICAL PROPERTIES

Bulk blanks for mechanical property test specimen were machined from the pancakes. After heat treatment, the specimens were finish-machined into 5.72 cm (2.25 in.) long Army

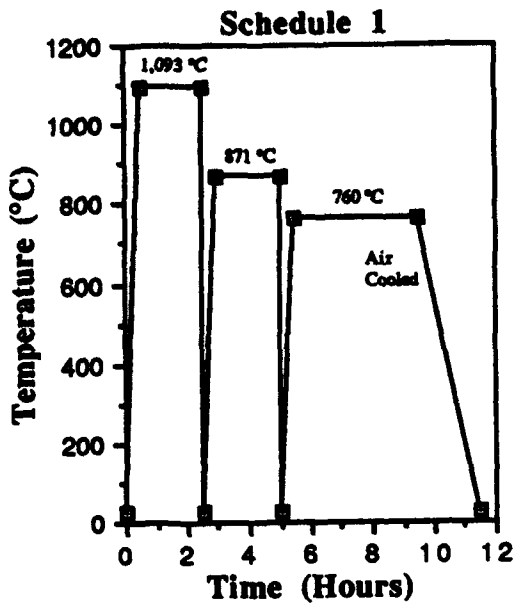

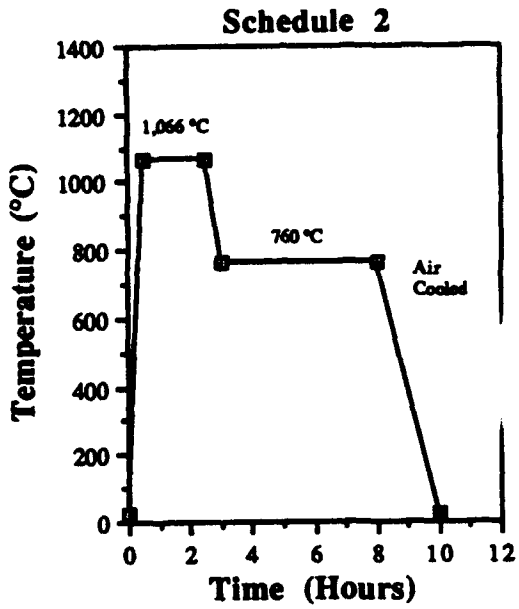

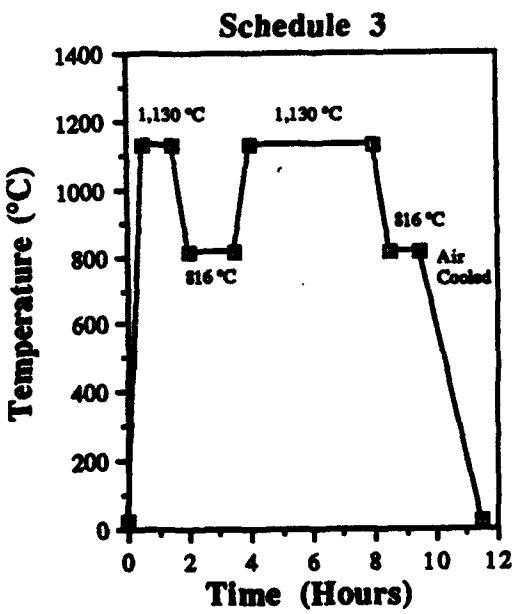

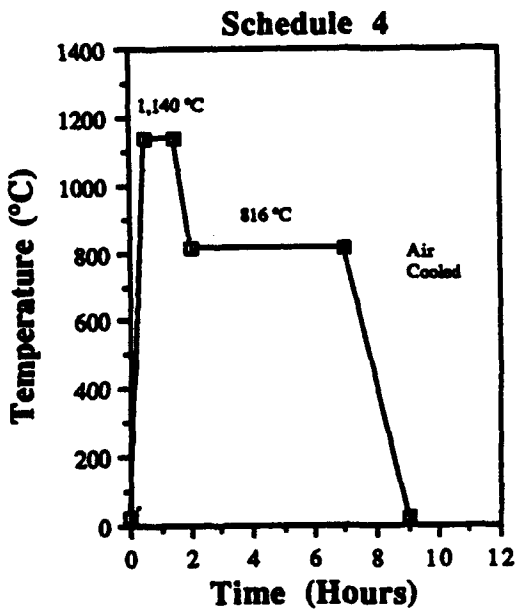

Figure. 10. Plots of heat treatment schedules.

Figure. 11. Microstructure of a sample heat treated by schedule 1, revealing scattered areas of primary α_2 in the α_2/β matrix.

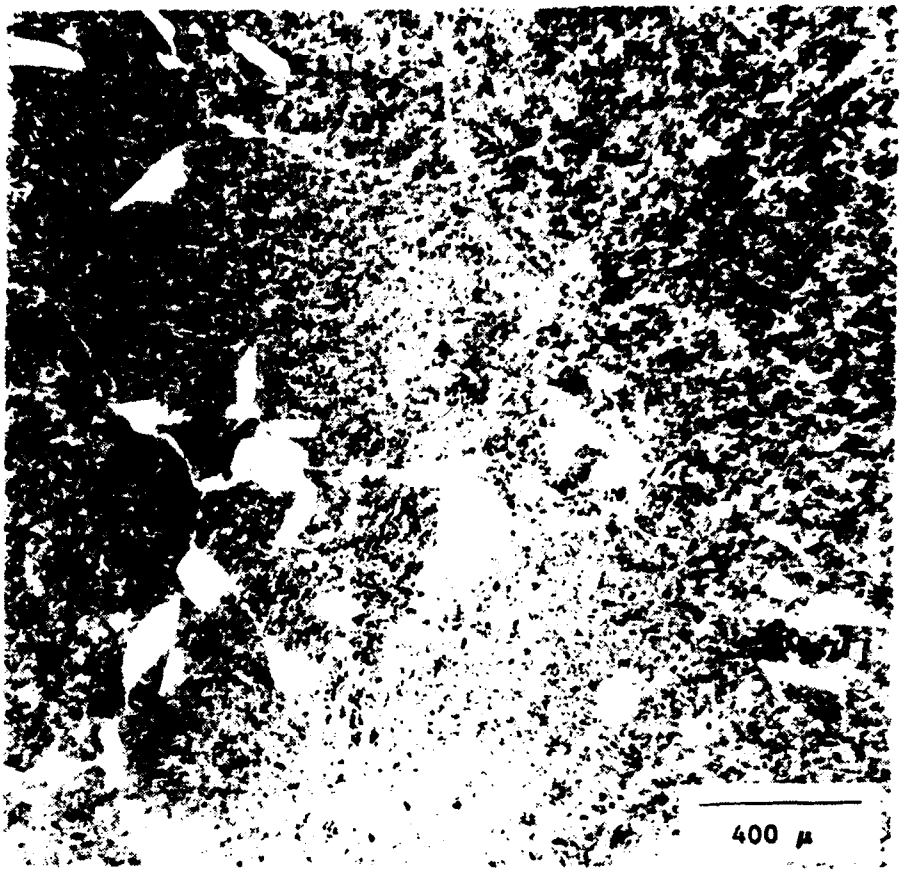

Figure. 12. Optical micrograph of a sample heat treated by schedule 2 showing a mixed structure of equiaxed primary α_2 and α_2/β matrix.

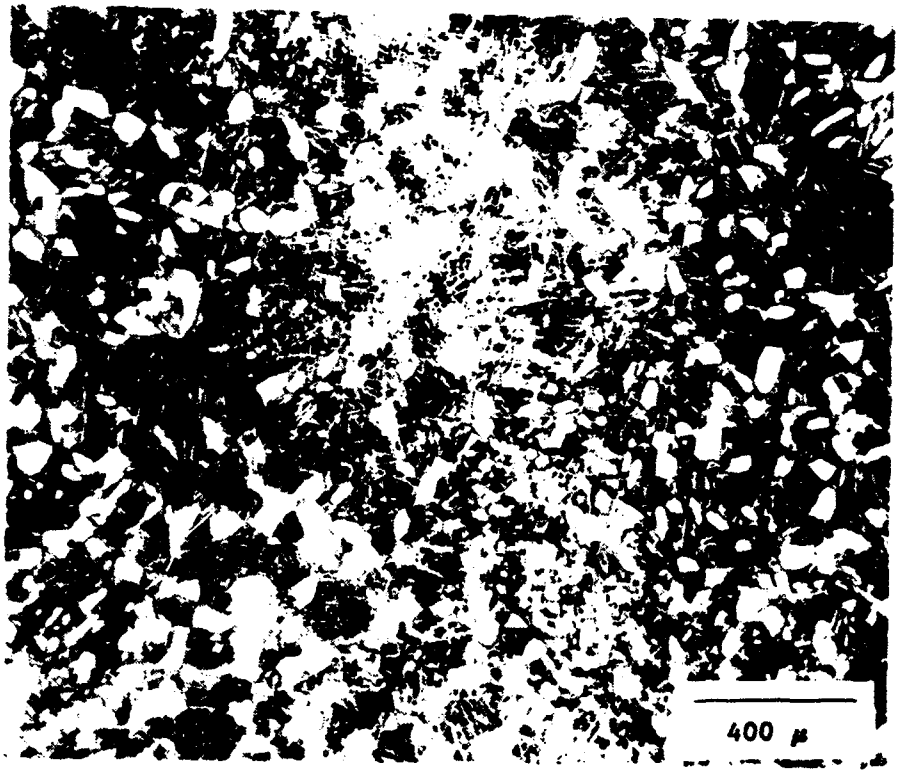

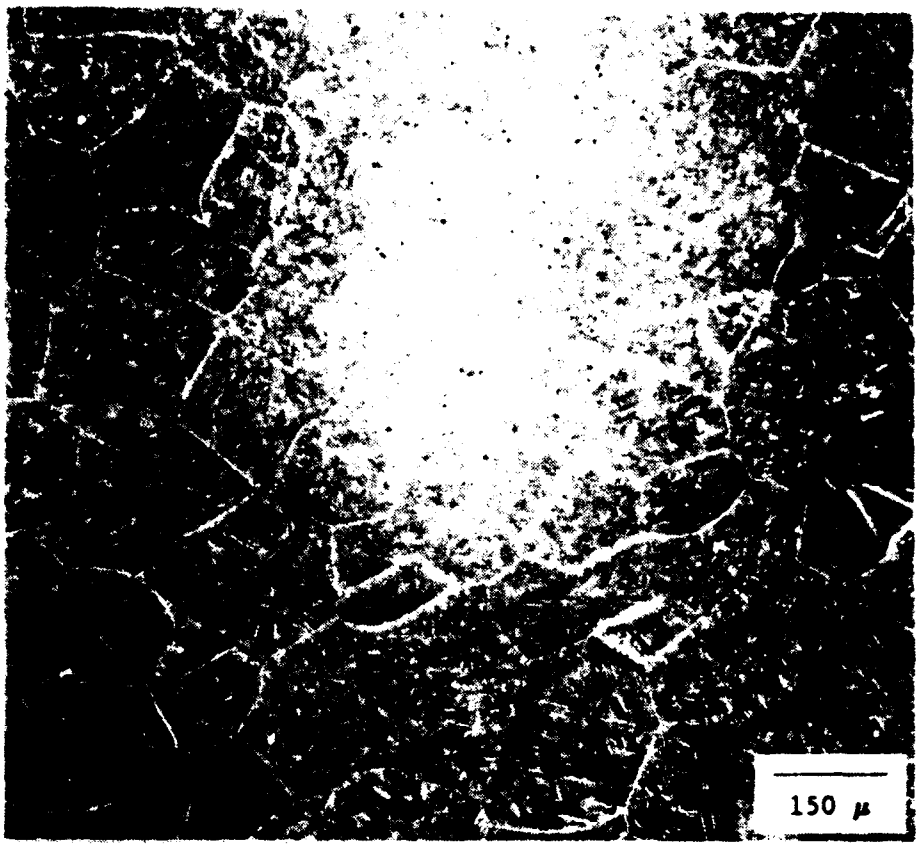

(a)

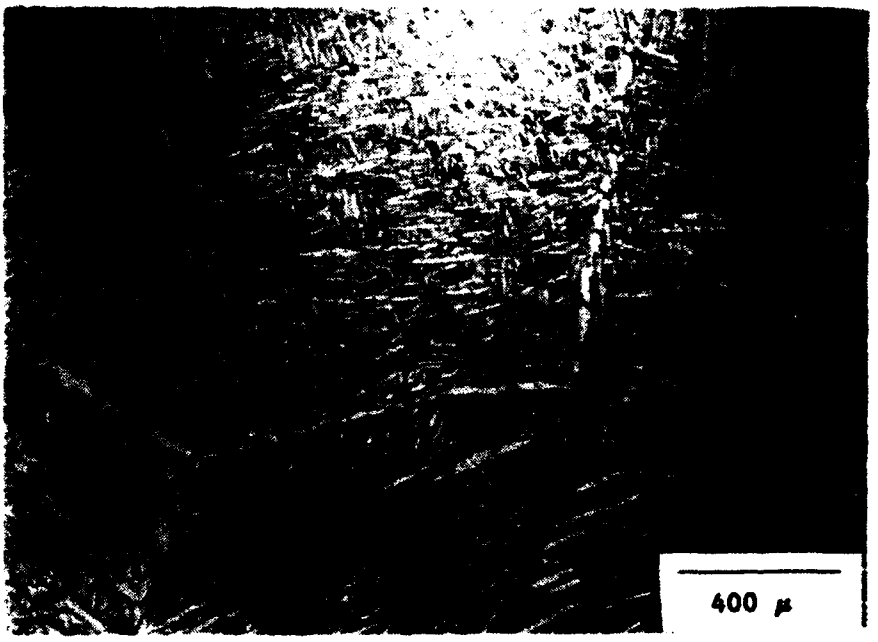

(b)

Figure. 13. Plate-like α_2 phase in a sample heat treated by schedule 3, showing (a) a transformed colony-type α_2 structure, and (b) fine acicular α_2/β matrix with coarse α_2 present at the prior β grain boundaries.

Figure. 14. Fine Widmanstatten structure with clearly defined β grain boundaries observed in a sample heat treated by schedule 4.

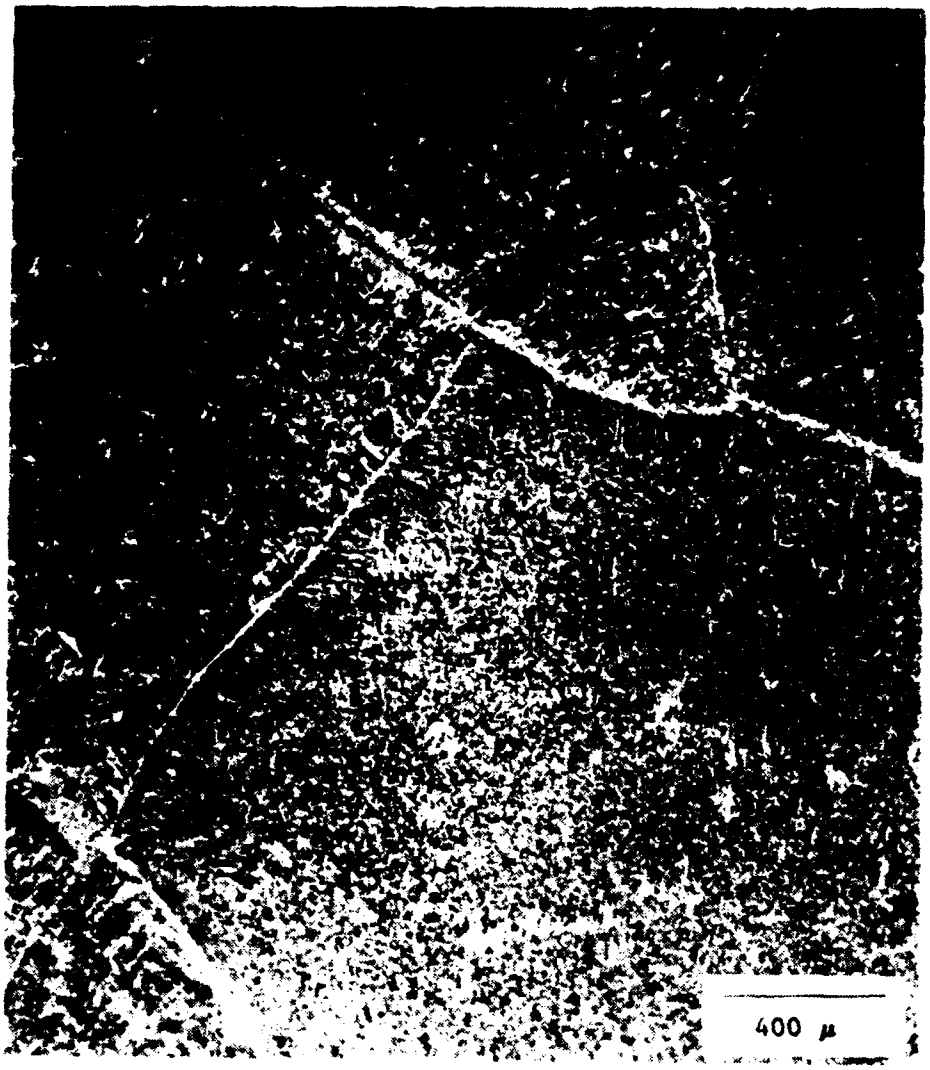

Research Laboratory-Materials Directorate (ARL-MD) standard TR-5 tensile specimens and 5.40 cm (2.125 in.) long ARL-MD standard TRC-6 tension creep specimens, as shown in Figure 15 [20]. Room temperature tensile tests were performed on specimens for each of the four heat-treatment conditions as well as the as-ROC'ed material using a 88,964 N (20 kip) capacity Instron with a 22,241 N (5,000 lb) load cell and a crosshead speed of 0.127 cm/min (0.05 in/min). Tensile tests were also performed at 427°C (800°F). Stress rupture testing was performed on a 44,482 N (10,000 lb) capacity stress rupture machine at a temperature of 649°C (1,200°F) with a stress of 379 MPa (55 ksi). For the stress rupture test, specimens were brought to temperature and held for approximately 30 minutes before the load was applied. Table 5 summarizes the measured mechanical properties.

Table 4. Heat treatment schedule and the resultant aspect ratio of α_2 phase

Heat Treatment	Schedule	Average Aspect Ratio
φ	as-received (as-ROC'ed)	3
1	1,093°C (2,000°F) x 2hr + water quenched + 871°C (1,600°F) x 2hr + water quenched + 760°C (1,400°F) x 4hr + air cooled	6
2	1,066°C (1,950°F) x 2 hr + 760°C (1,400°F) x 5 hr + air cooled	9
3	1,130°C (2,066°F) x 1 hr + 816°C (1,500°F) x 1.5 hr + 1,130°C (1,500°F) x 1 hr + air cooled	10
4	1,140°C (2,084°F) x 1 hr + 816°C (1,500°F) x 4 hr + air cooled	5

Table 5. Mechanical properties

Specimen	0.2% YS (ksi)	UTS (ksi)	%RA	%El	Time To Failure (hour)
Room Temperature Tensile					
φA	668.8 (97.0)	857.7 (124.4)	2.5	<2	
1A	797.8 (115.7)	926.0 (134.3)	<2	<2	
2A	780.5 (113.2)	986.0 (143.0)	2.5	<2	
3A	617.8 (89.6)	848.8 (123.1)	6.5	<2	
4A	977.7 (141.8)	1,174.9 (170.4)	<2	<2	
427°C (800°F) Tensile					
φB	497.1 (72.1)	861.2 (124.9)	22.9	24.3	
1B	591.6 (85.8)	1,042.5 (151.2)	22.1	19.3	
2B	641.9 (93.1)	919.1 (133.3)	18.1	15.4	
3B	406.1 (58.9)	792.9 (115.0)	25.4	22.8	
4B	711.6 (103.2)	1,139.1 (165.2)	7.5	6.7	
Stress Rupture at 649°C/379 MPa (1,200°F/55 ksi)					
φC			18.3	8.0	8.2
1C			10.1	10.0	37.6
2C			10.7	9.1	31.3
3C			10.1	9.7	20.0
4C			6.8	NA	33.7

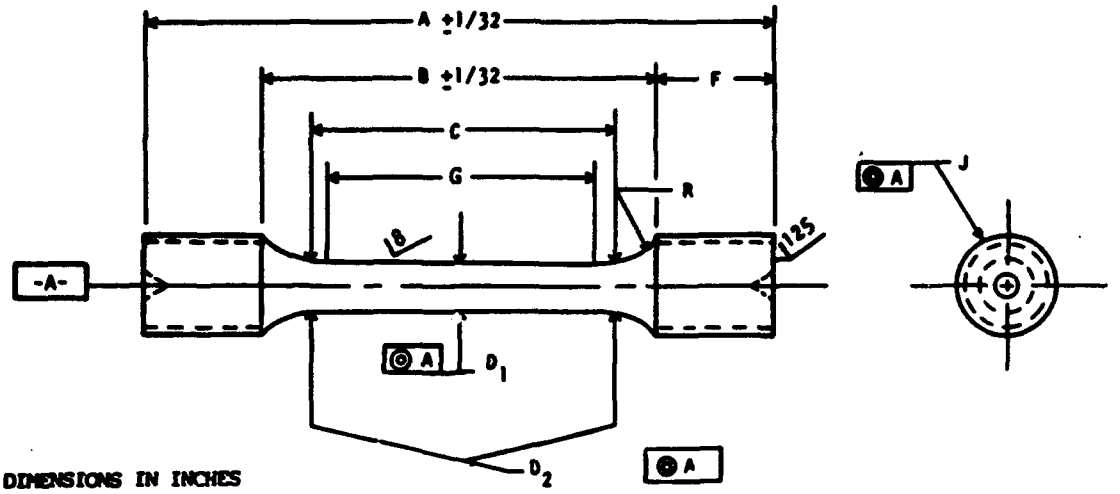

TYPE	A	B	C	D_1	D_2	G	F	J	R
TR 5	2-1/4	1-1/4	1-3/4	.160	.162	.64	1/2	5/16-24-2A	1/8

(a)

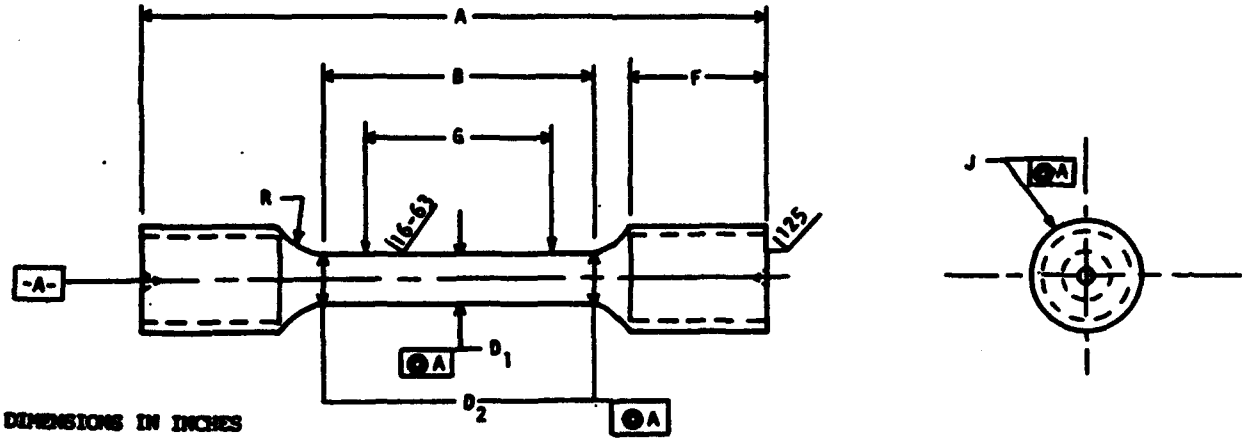

TYPE	A	B	G	D_1	D_2	F	J	R
TRC 6	2-1/8	1-1/8	.45	0.113	0.114	13/32	1/4-20-2A	3/32

(b)

Figure. 15. Specimen dimensions (a) ARL-MD TR-5 tensile specimen, and (b) ARL-MD TRC-6 tension creep specimen [20].

For sample 4A heat treated by schedule 4, the unusually high yield strength (YS) and ultimate tensile strength (UTS), 977.7 and 1,174.9 MPa (141.8 and 170.4 ksi), were accompanied by poor room temperature ductility, <2%; this is a consequence of the presence of the fine acicular α_2 phase. The tensile strength is compromised when the acicular α_2 coarsens, while room temperature ductility improves as indicated by sample 3A, having a YS and a UTS of 617.8 and 848.8 MPa (89.6 and 123.1 ksi), respectively, and a reduction of area (RA) of 6.5%. The mixed structure of fine acicular transformed α_2 and equiaxed primary α_2 for sample 2A, as shown in Figure 12, provides a better tensile strength than specimen 3A but reduced ductility; note the higher YS and the UTS values, but the decreased RA.

The tensile properties at elevated temperature follow a trend similar to the room temperature properties. Samples 4A and 4B show the highest tensile strength at both room and high temperatures, but the lowest ductility. The ductility increases significantly for samples 3A and 3B compared with 4A and 4B because the acicular α_2 phase has coarsened. An interesting conclusion can be drawn regarding the mechanical properties and the morphology of the α_2 phase. Under otherwise similar conditions, ductility increases as the aspect ratio increases but the tensile strength is inversely related to the aspect ratio of the acicular α_2 phase at both temperatures considered. Evidence of these observations is given by Figures 13 and 14 and the comparison between the tensile strengths between samples 3A & 4A, and 3B & 4B. The inferior tensile strength of samples 1A and 2A compared with 4A is attributable to the coarse primary α_2 phase. It is also interesting to compare the properties and microstructure of samples φA and 3A or φB and 3B. The as-ROC'ed material shows a roughly equiaxed primary α_2 structure, as shown in Figure 5, compared with a much more plate-like structure in the sample heat treated by schedule 3, as shown in Figure 13. Despite the coarse microstructure found in the as-ROC'ed material, the φA and φB samples demonstrate better YS and UTS at both room and elevated temperatures, with lower ductility. This further supports the idea that the geometrical shape, i.e., aspect ratio, has a profound effect on the tensile properties and can, at least sometimes, outweigh the effect of refined microstructure.

The stress rupture properties obtained in this study and shown in Table 5 are remarkable. Three samples 1C, 2C and 4C had a failure time over 30 hours when tested at 649°C (1,200°F) and 379 MPa (55 ksi). Sample 3C had a relatively shorter failure time 20.0 hours. It is also noteworthy that all samples show relatively good ductility; the RA values for samples 1C, 2C and 3C are all above 10% with the elongation values also ranging from 9.1 to 10.0%. The as-ROC'ed sample had a lower resistance to stress rupture because of the coarser primary α_2 microstructure.

FRACTURE MECHANISMS

Figures 16 and 17 show longitudinal (i.e. parallel to the load axis) cross section microstructures of tensile specimens tested at 427°C (800°F). They both show a flat transverse fracture surface with very limited secondary cracks immediately underneath the fracture surface indicating a single dominant crack. For the as-ROC'ed sample, as shown in Figure 16, a number of transverse cracks were nucleated along the specimen surface in the vicinity of the fracture surface. Most of them were short and randomly distributed indicating no preferential nucleation sites. More transverse cracks evenly distributed on the outer specimen surface were also observed for samples heat treated by schedule 2. In contrast to the as-ROC'ed specimen, the transverse cracks also occurred farther away from the fracture surface indicating a dual deformation process was present during the test. The first is uniformly distributed throughout the specimen in the longitudinal direction, nucleating cracks and contracting specimen diameter almost up to the shoulders of the specimen; the second is a localized necking process only observed in the vicinity of the final fracture surface as shown in Figure 17. In addition, a large number of irregularly shaped cavities, ranging from spherical to elongated, nucleated within the specimen for both as-ROC'ed and heat-

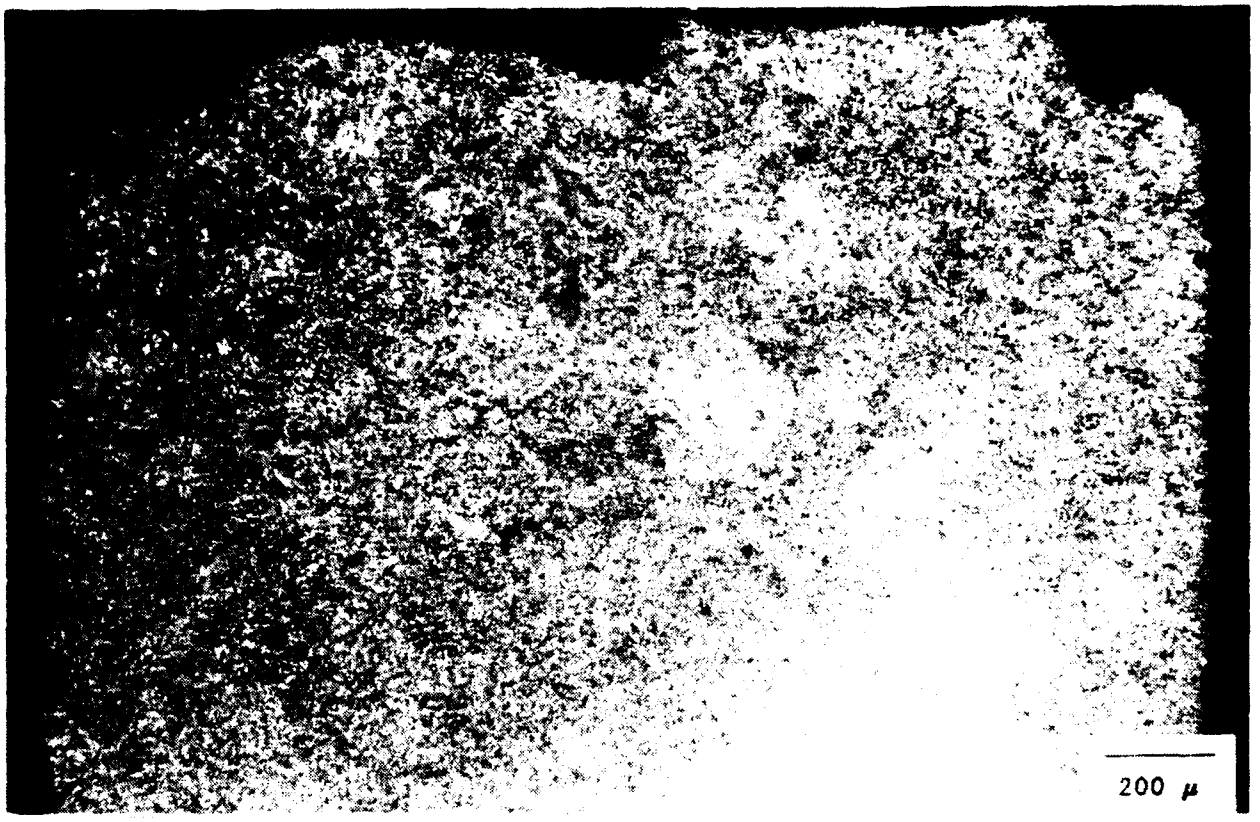

(a)

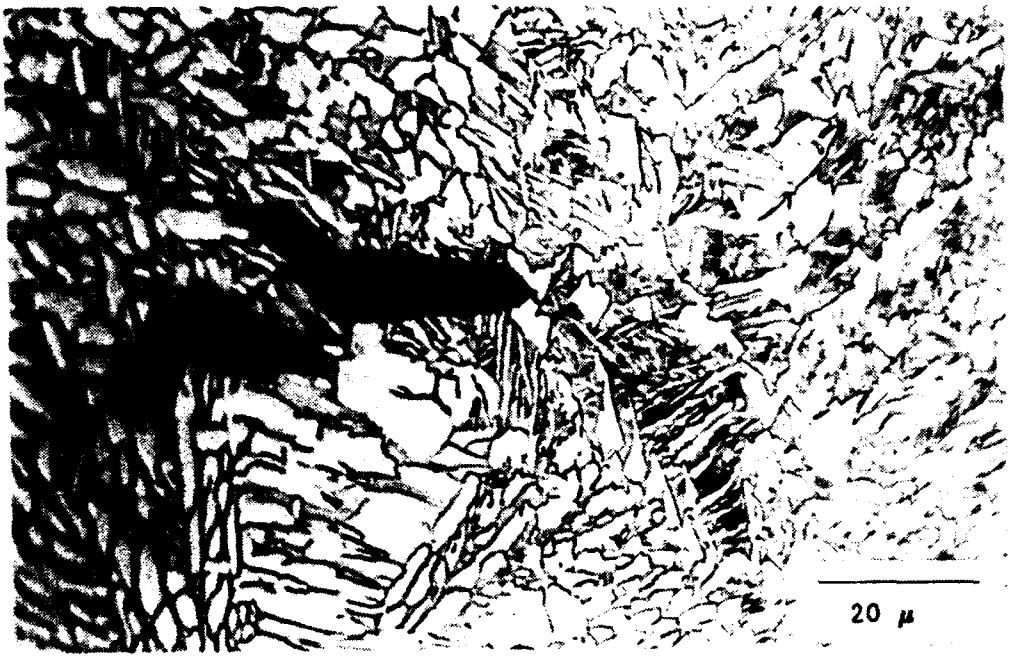

(b)

Figure. 16. Longitudinal cross section of a failed tensile specimen as-ROC'ed and tested at 427°C (800°F), showing (a) flat transverse fracture surface, with multiple transverse cracks in the longitudinal direction on the specimen surface and microvoids nucleated within the specimen, and (b) bridging of two cracks at the same horizontal plane.

Figure. 17. Microstructure of a failed tensile specimen heat treated by schedule 2 and tested at 427°C (800°F), showing a necked, flat fracture surface and multiple transverse cracks on the outer specimen surface.

treated (by schedule 2) specimens. These crack nucleations sites occurred in several phase morphologies.

Figure 18 shows a longitudinal cross-section microstructure of an as-ROC'ed stress rupture specimen tested at 649 °C/379 MPa (1,200 °F/55 ksi) that broke after 8.2 hours. During the test multiple transverse cracks nucleated both on the specimen surface (edge) and within the specimen. No longitudinal cracks were detected (see Figures 18 and 19). Most transverse cracks nucleated at the specimen surface are due to relatively high stress concentration resulting from surface roughness (in contrast to the interior smoothness). These surface cracks grow competitively in the transverse direction and some eventually coalesce with outwardly growing interior cracks to produce final failure. Despite the fact that the interior cracks were few in number and scattered, some are actually fracture-controlling because the "small" surface cracks have to coalesce with interior cracks to reach the critical crack length for propogation leading to failure. No preferential crack nucleation sites were observed. As shown in Figure 20, one large crack on the the left side was initiated in the fine α_2/β matrix, the middle crack was initiated on the interior boundary (interface) between coarse primary α_2 phase and fine α_2/β matrix, the third major crack on the right side was initiated in a cluster of coarse α_2 phase. The crack propagation rate is seemingly slow as indicated by the short length of surface cracks and is about the same no matter where they were nucleated. The failure is controlled by the interior crack nucleation and the subsequent linkage between the interior and surface cracks. When multiple cracks happen to nucleate in the same plane in the specimen, they will soon coalesce together and reach the critical length leading to the final fracture. The grain boundaries of prior β grains were not necessarily favorite crack nucleation sites nor preferred paths for crack propagation as shown in Figure 21.

Similar conclusions can also be drawn from Figure 22. Cracks were randomly nucleated throughout a variety of microstructure morphologies. The frequency of crack nucleation and the subsequent crack propagation rate are about the same among coarse primary α_2 phase, fine α_2/β matrix, prior β grain boundary and the boundaries (interfaces) between these various phases. Crack nucleation and propagation were predominantly affected by the direction of stress (i.e. tension) and stress concentration, and not the different cohesive strength of various metallurgical phases and constituents.

Table 6 summarizes the fractographic features of specimens tested in various conditions. The prior β grain size for a post-tested specimen is about the same as before the test for both tensile and stress rupture specimens. In the stress rupture specimen, microvoids nucleated during the test at elevated temperature and subsequently coalesced to form the colonies as shown in Figures 23 and 24. The colony size observed in the scanning electron microscopy (SEM) fractographs is about 200 μm, about five times larger than the prior β grain size. This indicates that the stress rupture test nucleates multiple cracks (in several prior β grains) which grow simultaneously and eventually bridge together resulting in final fracture. The nucleation and coalescence of microvoids are heavily dependent on temperature, stress and the exposure time period exposed to these elevated temperatures and high stresses. The colony-type fracture is less well defined for tensile tests at 427°C (800°F) as shown in Figures 25 and 26. Ductile dimples and microvoids are still visible in these tensile specimens, however a shear river fracture pattern also appears. The fracture surfaces of room temperature tensile specimens as-ROC'ed show predominantly shear river fracture pattern - no microvoid or colonies can be observed. However, for a sample heat treated by schedule 2, large (about 300 μm) but vaguely defined colonies on the fracture surface were observed as shown in Figures 27 and 28. These variations are attributable to the different starting microstructures. The as-ROC'ed specimen, as shown in Figure 5, starts with a primarily coarse α_2 structure with vaguely defined β grains. On the other hand the microstructure of the specimen heat treated by schedule 2, as shown in Figure 11, has a mixture of well defined β grains and primary α_2 phase.

Figure. 18. Longitudinal cross section of a failed stress rupture specimen as-ROC'ed, showing multiple transverse cracks.

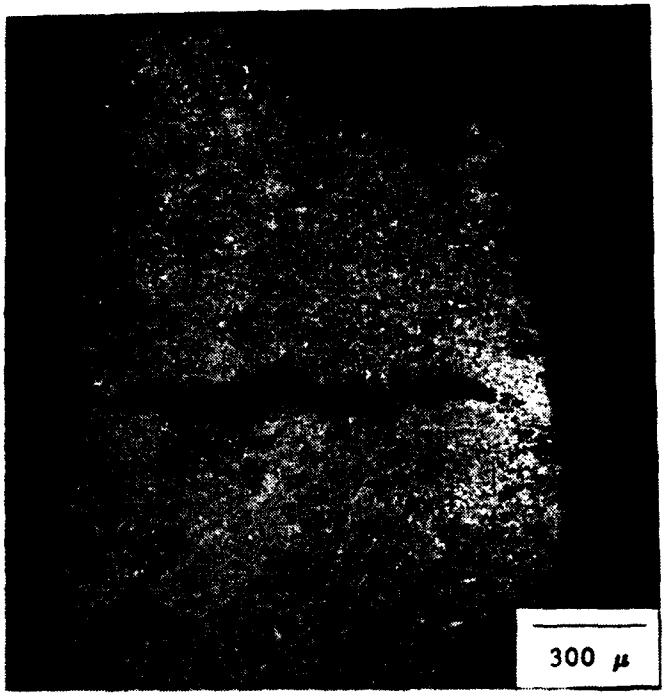

Figure. 19. Transverse fracture surface of a failed stress rupture specimen as-ROC'ed, showing no longitudinal cracks.

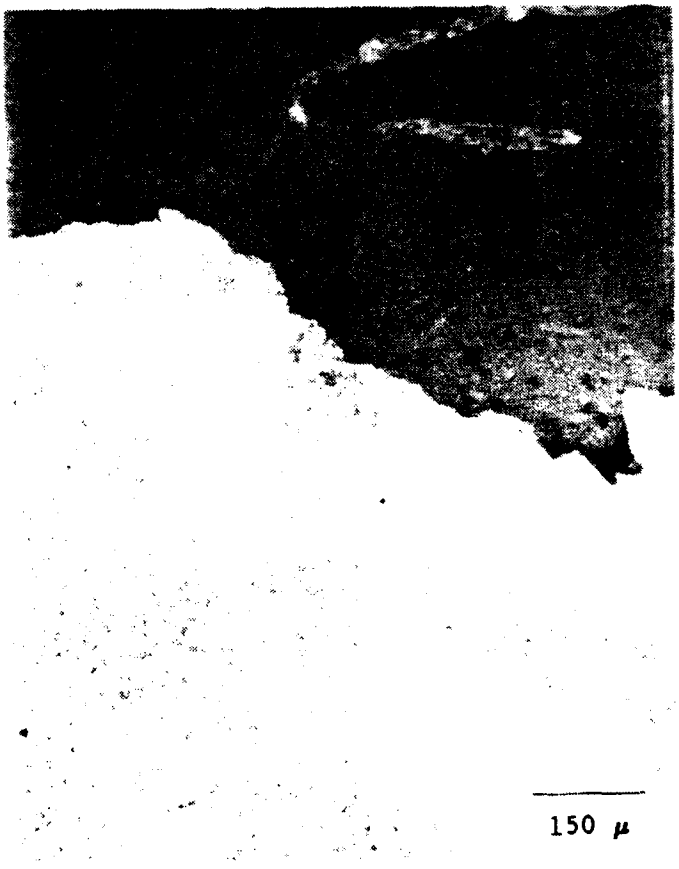

Figure. 20. Transverse surface cracks observed in an as-ROC'ed stress rupture specimen, showing no preferential crack nucleation sites.

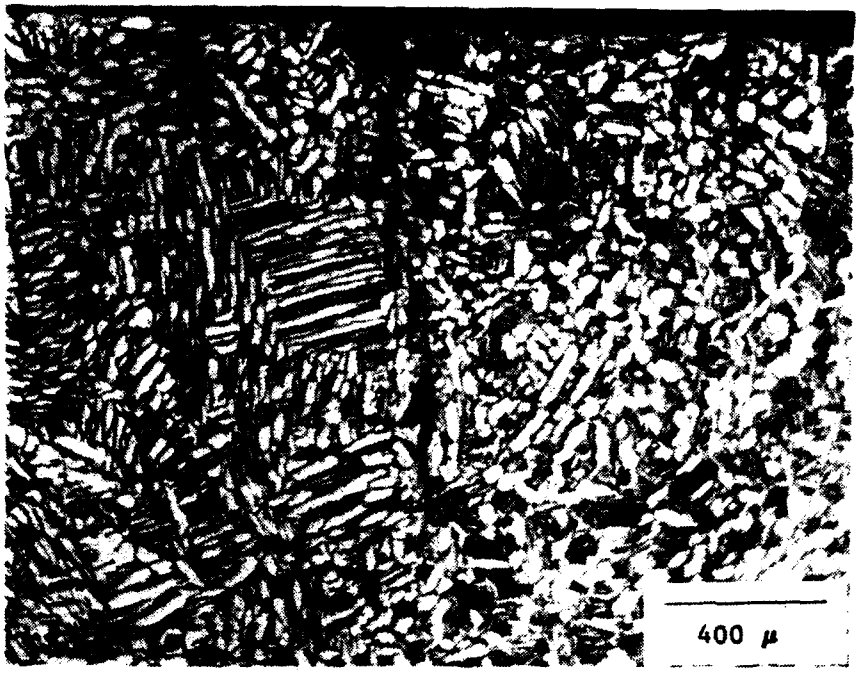

Figure. 21. Crack coalescence observed in an as-ROC'ed stress rupture specimen.

Figure. 22. Randomly nucleated cracks observed in an as-ROC'ed stress rupture specimen.

Table 6. Features of fractographs

Specimen	SEM	Optical
φB (Tensile at 427°C/800°F)	shear river pattern, ductile dimples, microvoids	several transverse cracks along the specimen surface near the fracture cross-section and irregular cavities within the specimen
φC [Stress rupture at 649°C/379 MPa (1,200°F/55 ksi)]	transgranular colony-type fracture, colony size ≈200 μm	multiple transverse cracks randomly nucleated, prior β grain size ≈ 40 μm
2A (Tensile at RT)	large but vaguely defined transgranular colony-type fracture, colony size ≈ 300 μm	-
2B (Tensile at 427°C/800°F)	mixture of transgranular colony-type & intergranular shear fracture, microvoids	a number of transverse cracks along the surface & irregular cavities within the specimen
2C [Stress rupture at 649°C/379 MPa (1,200°F/55 ksi)]	mixture of transgranular colony-type (interior) and intergranular shear (surface/edge) fracture , microvoid coalescence	-

Figure. 23. SEM fractographs of an as-ROC'ed stress rupture specimen, showing a) overall view of colony-type fracture, (b) microvoids, and (c) close-up examination at higher magnification.

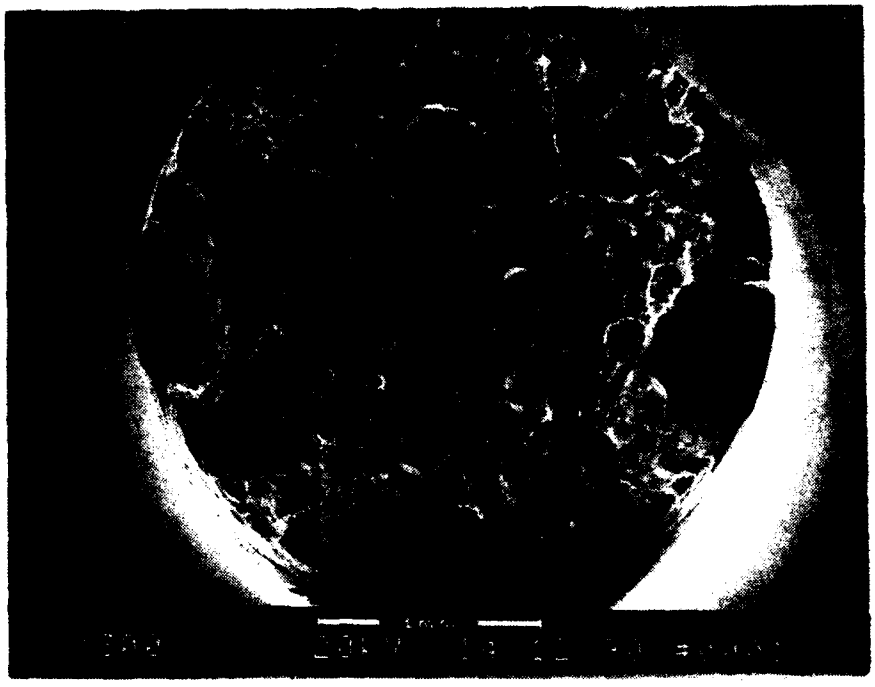

(a)

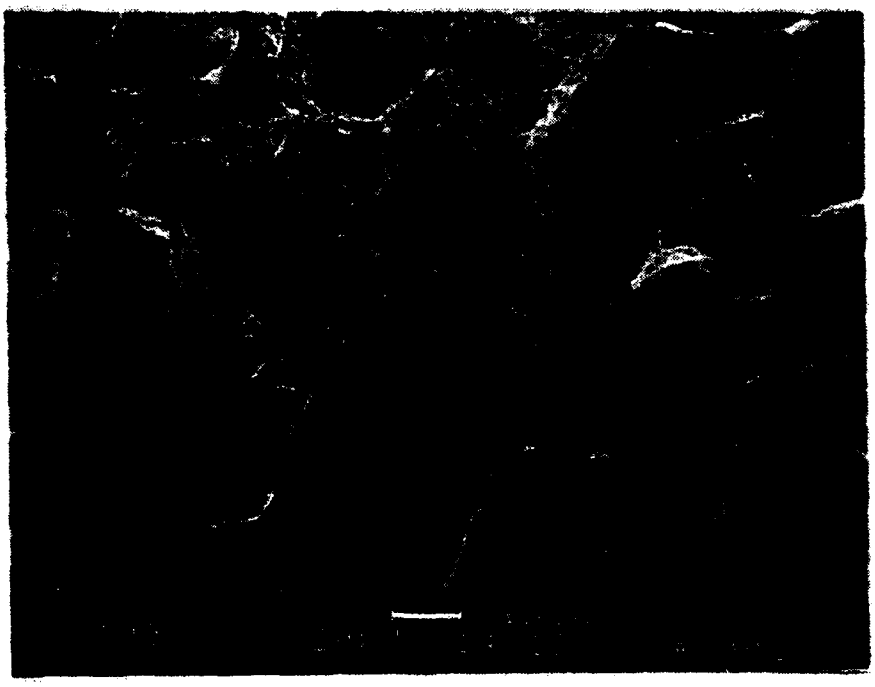

(b)

Figure. 23. SEM fractographs of an as-ROC'ed stress rupture specimen, showing a) overall view of colony-type fracture, (b) microvoids, and (c) close-up examination at higher magnification.

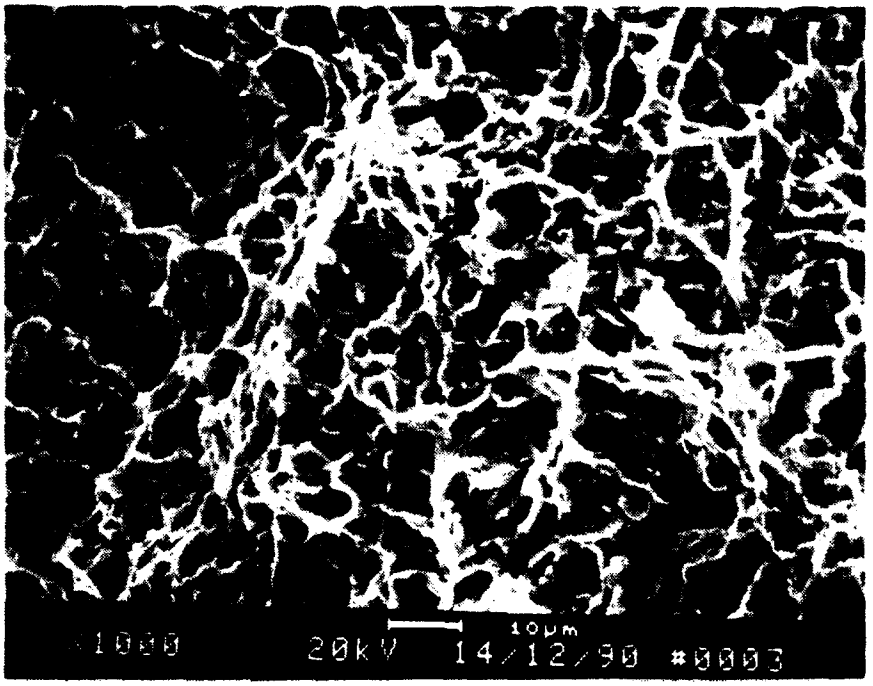

(c)

Figure. 24. SEM fractographs of a stress rupture sample heat treated by schedule 2, showing (a) mixture of colony-type (center) and shear (edge) fracture, (b) microvoids, and (c) close-up examination at higher magnification.

(a)

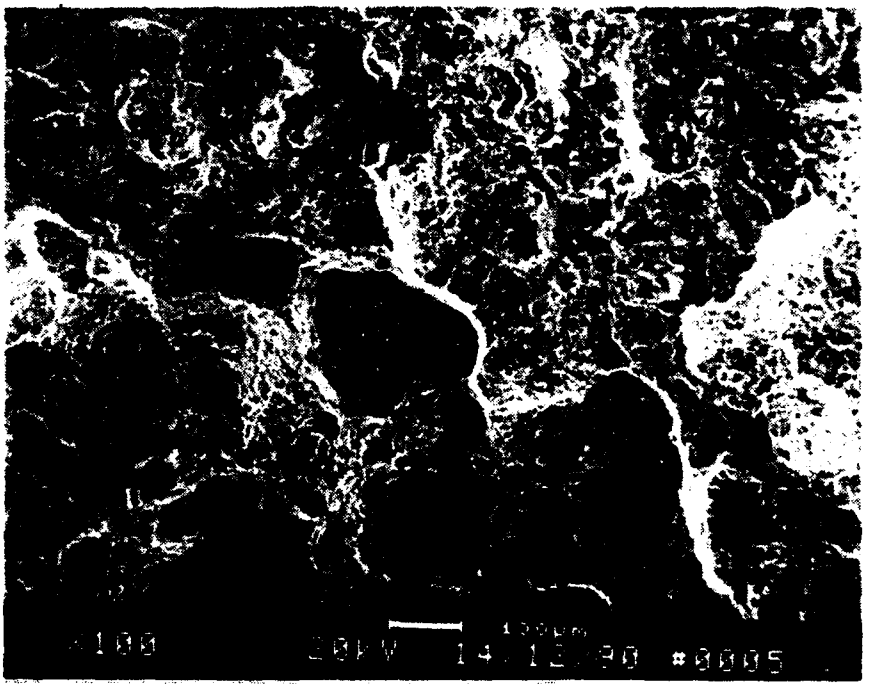

(b)

Figure. 24. SEM fractographs of a stress rupture sample heat treated by schedule 2, showing (a) mixture of colony-type (center) and shear (edge) fracture, (b) microvoids, and (c) close-up examination at higher magnification.

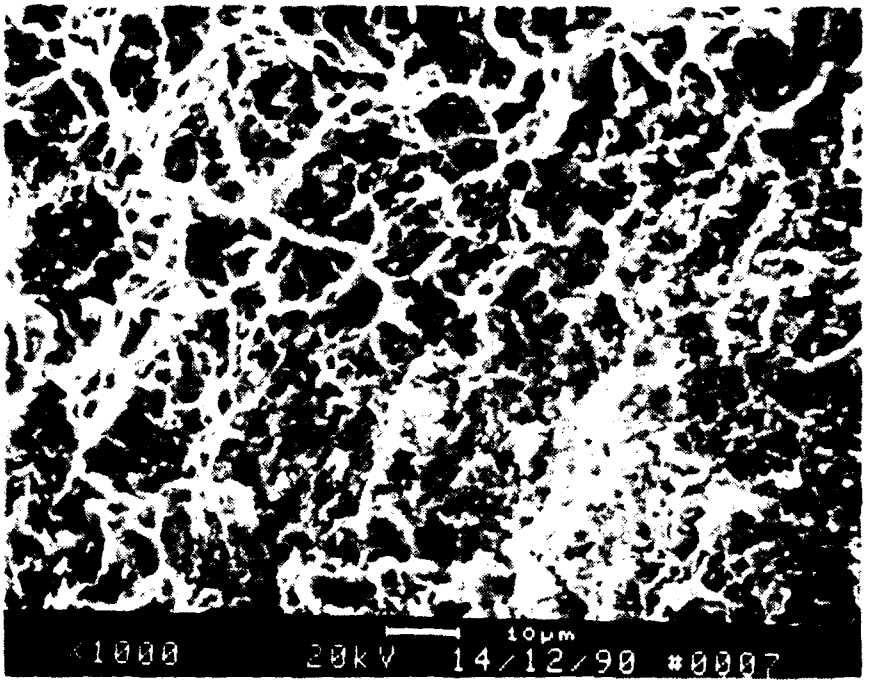

(c)

Figure. 25. SEM fractographs of an as-ROC'ed tensile specimen tested at 427°C (800°F), showing (a) vaguely defined colonies, (b) mixture of microvoids and shear fracture, and (c) close-up examination at higher magnification.

(a)

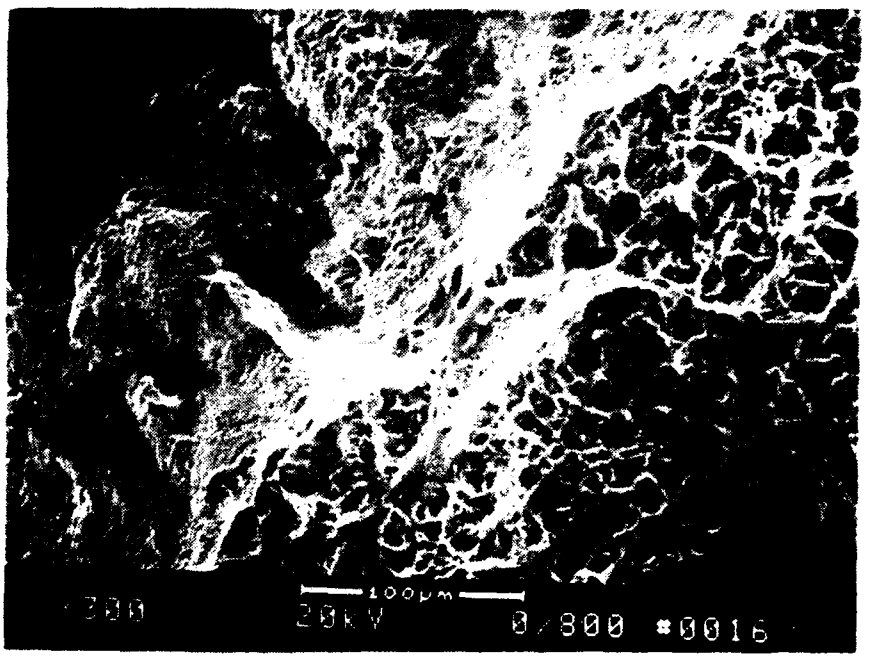

(b)

Figure. 25. SEM fractographs of an as-ROC'ed tensile specimen tested at 427°C (800°F), showing (a) vaguely defined colonies, (b) mixture of microvoids and shear fracture, and (c) close-up examination at higher magnification.

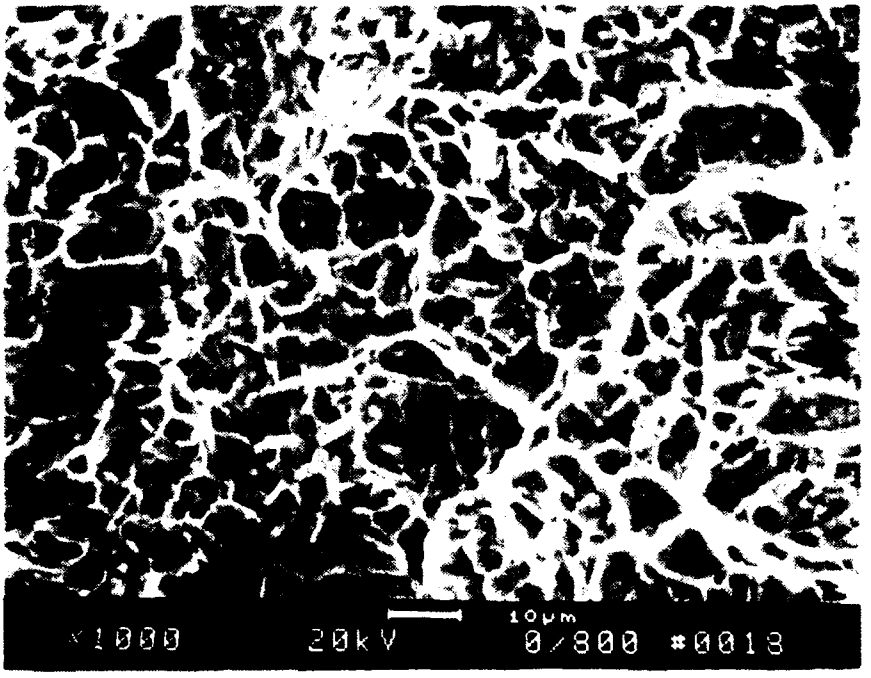

(c)

Figure. 26. SEM fractographs of a tensile sample heat treated by schedule 2, tested at 427°C (800°F), showing (a) mixture of transgranular colony-type and intergranular shear fracture, and (b) close-up examination at higher magnification.

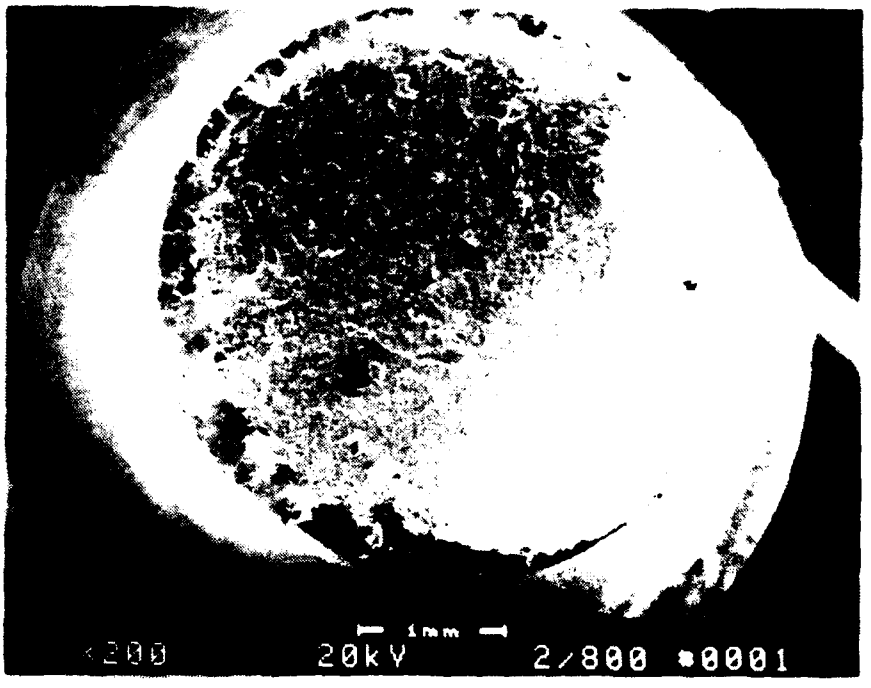

(a)

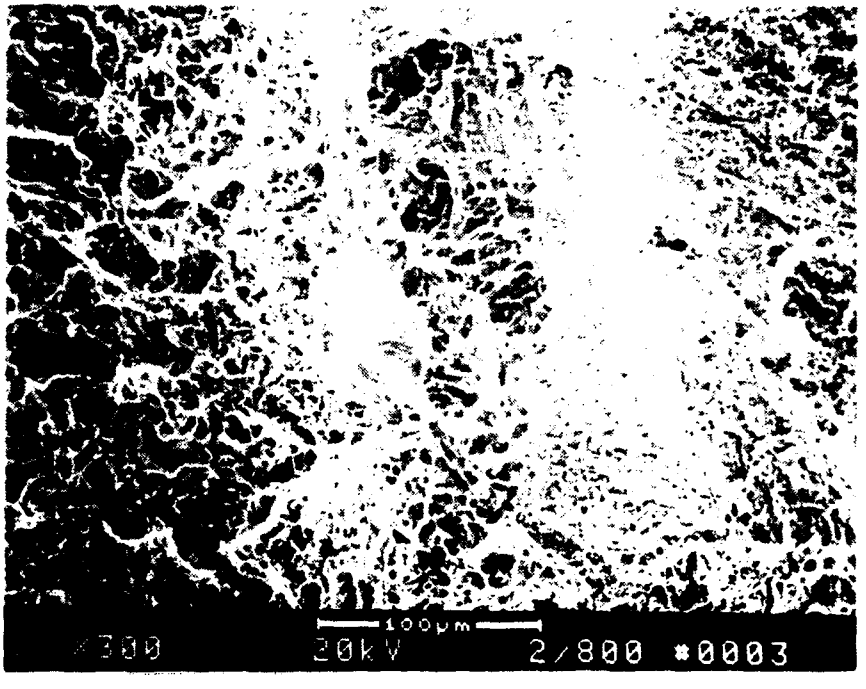

(b)

Figure. 27. SEM fractographs of an as-ROC'ed tensile specimen tested at room temperature, showing (a) overall fracture pattern, and (b) shear fracture.

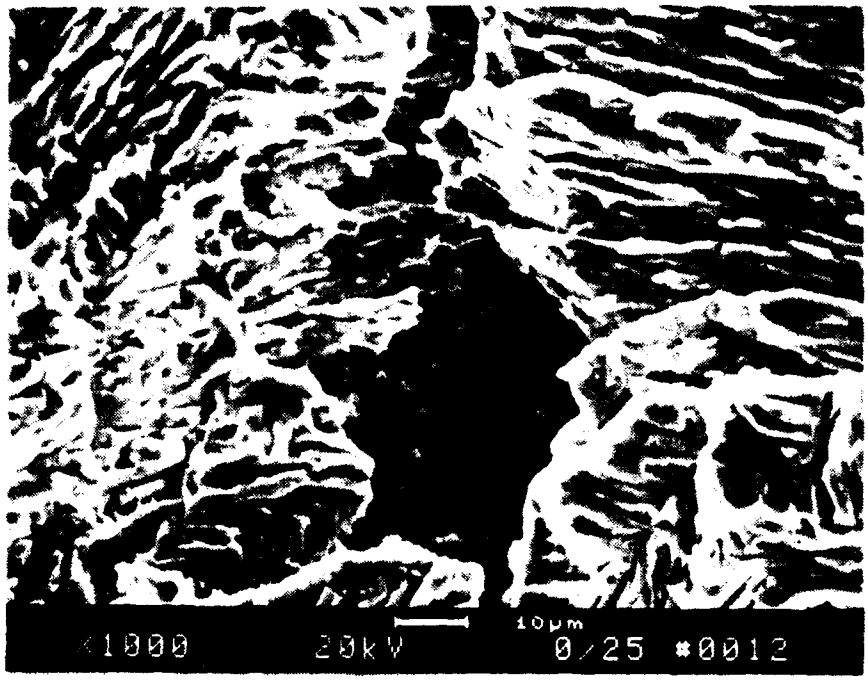

(a)

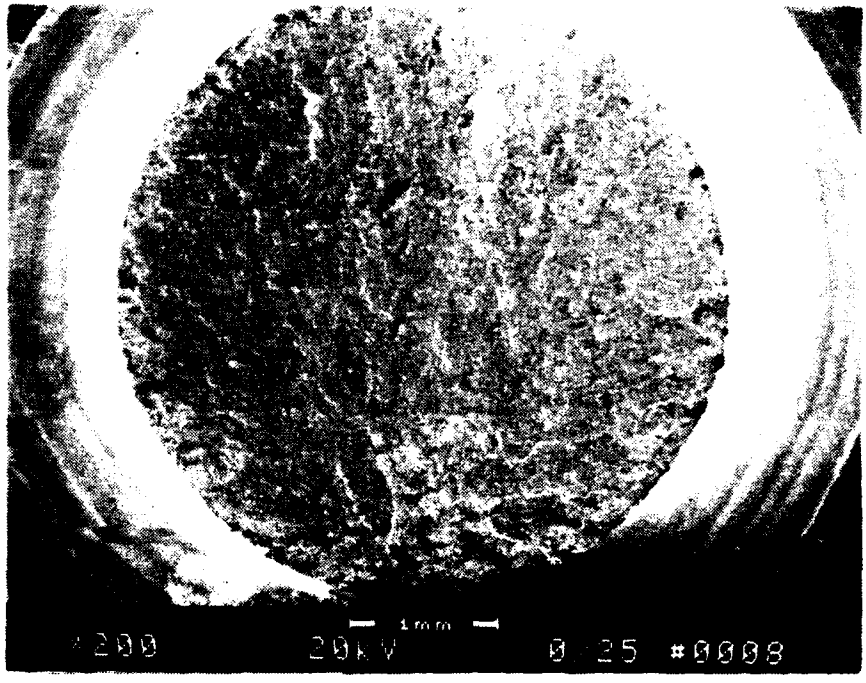

(b)

Figure. 28. SEM fractographs of a tensile specimen heat treated by schedule 2, tested at room temperature, showing (a) large but vaguely defined colony-type fracture, and (b) microvoids and shearing trace.

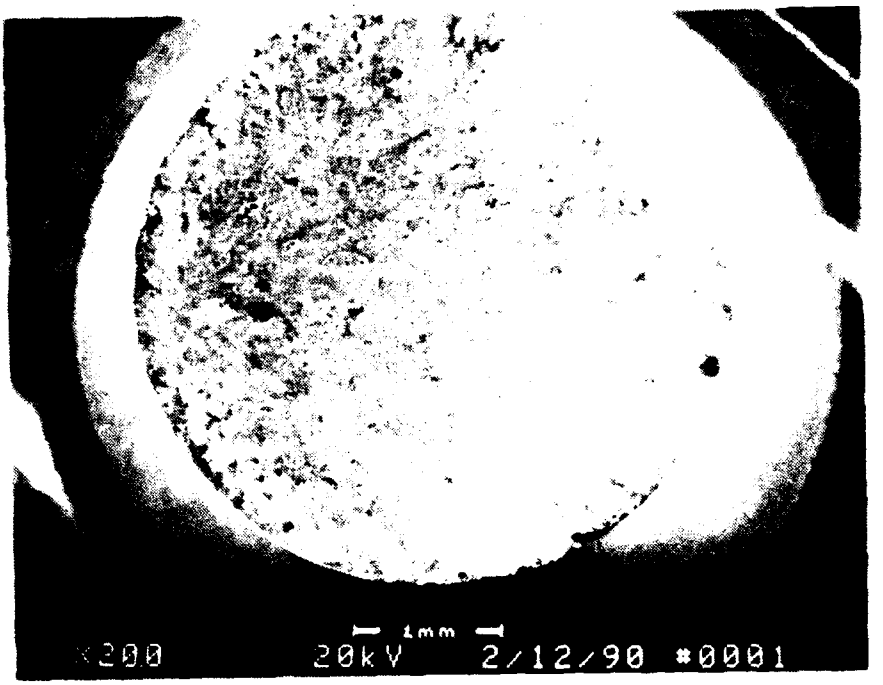

(a)

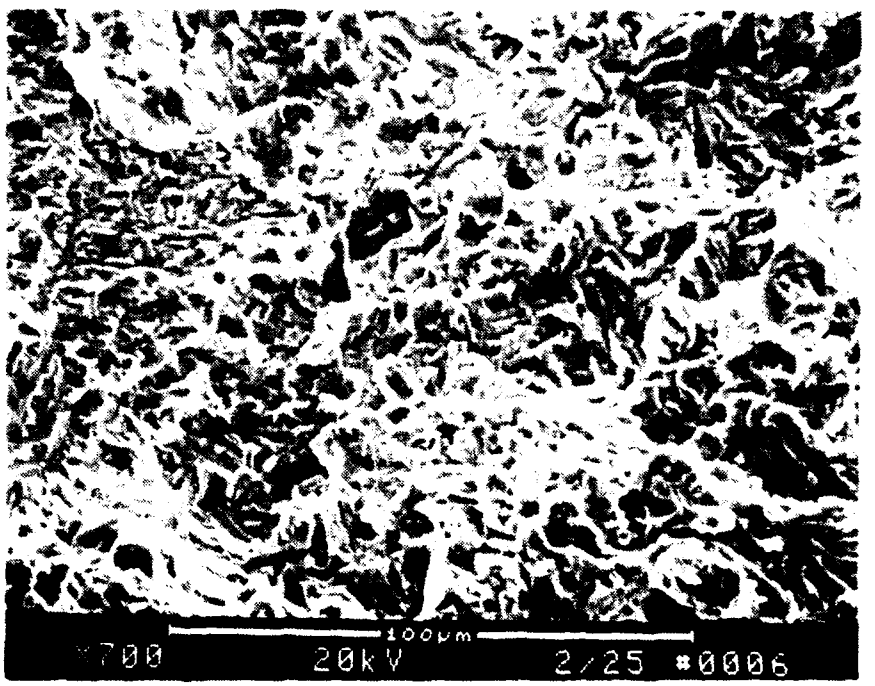

(b)

COMPARISON BETWEEN ROC'ED AND HIP'ED MATERIALS

A similar α_2 alloy modified with a minor addition of erbium (Er), Ti-25Al-10Nb-3V-0.3Er (at%), was converted to powder using the PREP technique from vacuum arc remelted (VAR) ingots in an earlier study [21]. This study found that the effect of Er is negligible. The powder was divided into three groups and subsequently consolidated by hot isostatic pressing (HIP) at temperatures of 900, 1,010 or 1,120°C (1,650, 1,850 or 2,050°F), for two hours at a pressure of 103.4 MPa (15 ksi). Following a series of heat treatments, the mechanical properties were evaluated at both room and elevated temperatures. At room temperature, the YS and the UTS range from 448.9 and 888.1 MPa (65.1 and 128.8 ksi), and 330.3 and 701.2 MPa (47.9 and 101.7 ksi), respectively; and the elongation values range from 0.5% to 5.9%.

The comparison between ROC'ed and HIP'ed alloys, as shown in Table 7, reveals that the ROC'ed material has much superior mechanical properties at both room and elevated temperatures. At room temperature the YS is about 50% higher and the RA is even more promising for the ROC'ed material compared with the HIP'ed counterpart, a maximum of 6.5 versus 2.6%. A similar conclusion can also be drawn at elevated temperature. For instance, the YS and the UTS for the ROC'ed material range from 406.1 to 711.6 MPa (58.9 to 103.2 ksi) and 792.9 to 1,139.1 MPa (115.0 to 165.2 ksi) versus 528.8 to 533.7 MPa (76.7 to 77.4 ksi) and 557.1 to 689.5 MPa (80.8 to 100.0 ksi), respectively, for the HIP'ed material. The most striking benefit of the ROC process comes from the improvement of ductility. At 427°C (800°F), the RA and elongation of the ROC'ed material range from 7.5 to 25.4% and 6.7 to 22.8% versus 1.3 to 5.8% and 0.1 to 5.9%, respectively, for the HIP'ed material. The stress rupture properties are also included in Table 7. The ROC'ed material has much superior stress rupture properties. The HIP'ed material virtually shows no resistance to stress rupture test at 649°C/397.2 MPa (1,200°F/55 ksi).

Table 7. Comparison between ROC'ed and HIP'ed Materials

Properties	ROC'ed Material	HIP'ed Material
Room Temperature Tensile		
0.2% YS	617.8 - 977.7	360.0 - 690.9
MPa (ksi)	(89.6 - 141.8)	(52.3 - 100.2)
UTS	848.8 - 1,174.9	408.9 - 841.9
MPa (ksi)	(123.1 - 170.4)	(59.3 - 122.1)
RA (%)	maximum 6.5	1.3 - 2.6
Elongation (%)	<2	0.2 - 1.1
427°C (800°F) Tensile		
0.2% YS	406.1 - 711.6	528.8 - 533.7
MPa (ksi)	(58.9 - 103.2)	(76.7 - 77.4)
UTS	792.9 - 1,139.1	557.1 - 689.5
MPa (ksi)	(115.0 - 165.2)	(80.8 - 100.0)
RA (%)	7.5 -25.4	1.3 - 5.8
Elongation (%)	6.7 - 22.8	0.1 - 5.9
Stress Rupture at 649°C/397.2 MPa (1,200°F/55 ksi)		
Time to failure (hours)	8.2 - 37.6	0 - 0.2
RA (%)	6.8 - 18.3	0 - 3.3
Elongation (%)	8.0 - 10.0	0.4 - 2.1

The inferior mechanical properties of the HIP'ed material can be partially attributed to a coarser microstructure, resulting from a longer exposure to high temperature, 2 hours versus 15 seconds, during the consolidation process.

SUMMARY AND CONCLUSIONS

A Ti-25Al-10Nb-3V-1Mo alloy prepared by ROC of prealloyed PREP powder shows superior mechanical properties when compared with HIP'ed material of similar composition. The ductility increases with an increasing aspect ratio of the α_2 phase, however, the strength is inversely related to the aspect ratio. In general, the plate-like α_2 phase provides a good combination of ductility and strength. The current alloy also demonstrates an excellent stress rupture resistance at elevated temperature. Multiple transverse cracks were randomly nucleated along the specimen surface and within the specimen during tensile and stress rupture tests. The stress rupture failure is controlled by the coalescence of microvoids and the bridging between simultaneously nucleated cracks on the same plane. Colony-type fracture was observed for stress rupture and tensile specimens with a β phase microstructure. For stress rupture and tensile specimens containing β phase, fracture occurred across colonies. The average colony size was usually five to seven times larger than the prior β grain size and resulted from the linkage of cracks in several β grains.

This project has helped to support the overall goals of developing new super high temperature materials applicable up to or even above 871°C (1,600°F) in the next decade.

ACKNOWLEDGMENT

This project was partially sponsored by the U.S. Army Aviation and Troop-support Command, Aviation Applied Technology Directorate, Fort Eustis, VA. The authors are indebted to Mrs. Marietta R. Scanlon for her help in experimental work, Mr. Paul Huang for his assistance in SEM and Mr. John Beck for his help in preparing the manuscripts. We are particularly grateful to Dr. Daniel Eylon for supplying the alloys and for his helpful discussions during the course of this study.

REFERNCES

1. Bassi, C., Peters, J.A., and Wittenauer, J. *Processing Titanium Aluminide Foils.* J. Metals, v. 41, no. 9, 1989, p. 18-20.

2. Froes, F.H. *Structural Aerospace Materials: The Right Stuff for the 21st Century.* Materials Edge, May/June, 1989, p. 17-44.

3. Sprague, R.A. *Future Aerospace-Materials Directions.* Advanced Materials and Processing 1, 1988, p. 67-73.

4. Kim, C.Y. J. of Metals, v. 42, July, 1989, p. 24-30.

5. Lipsitt, H.A. *High Temperature Ordered Intermetallic Alloys.* Mat. Res. Soc., 1985, p. 351-364.

6. Strychor, R., Williams, J.C., and Soffa, W.A. Metall. *Phase Transformations and Modulated Microstructures in Ti-Al-Nb Alloys.* Trans. v. 19A, 1988, p. 225-234.

7. Sastry, S.M.L., and Lipsitt, H.A. *Ordering Transformations and Mechanical Properties of Ti_3Al and Ti_3Al-Nb Alloys.* Metall. Trans., v. 8A, 1977, p. 1543-1552.

8. Edelson. L.H., and Ritchie, R.O. *Microstructural Characterization of α_2 + B2 Titanium Aluminide Intermetallic (Super-α_2) Using Transmission Electron Microscopy.* Mat. Sci. Eng., v. A130, 1990, p. 193-203.

9. Baeslack, W.A., and Broderick, T. *Effect of Cooling Rate on the Structure and Hardness of a Ti-26Al-10Nb-3V-1Mo Titanium Aluminide.* Script Metall., v. 24, 1990, p.319-324.

10. Aswath, P.B., and Suresh, S. *Fatigue Crack Growth Behavior of a Titanium Aluminide Intermetallic.* Mat. Sci. Eng., v. A114, 1989, p. L5-L10.

11. Ward, C.H., Williams, J.C., Thompson, A.W., Rosenthal, D.G., and Froes, F.H. *Fatigue Mechanisms in Titanium Aluminide Intermetallics.* Memoires et Etudes Scientifiques Revue de Metallurgie, v. 86, no. 10, 1989, p. 647-653.

12. Chan, K.S. *Fracture and Toughening Mechanisms in an α_2 Titanium Aluminide Alloy.* Metall. Trans., v. A21, 1990, p. 2687-2699.

13. Baeslack, W.A., Mascorella, T.J., and Kelly, T.J. *Weldability of a Titanium Aluminide.* Welding Journal, v. 68, 1989, p. 483s-498s.

14. Wittenauer, J., Bassi, C., and Walser, B. *Hot Deformation Characteristics of Nb-Modified Ti_3Al.* Scripta Metall., v. 23, 1989, p. 1381-1386.

15. Murray, J.L. *Calculation of the Titanium-Aluminum Phase Diagram.* Metall. Trans., v. 19A, 1988, p. 243-247.

16. Kim, Y.K., and Froes, F.H. *High Temperature Aluminide and Intermetallics.* AIME-TMS, 1989, p. 465-492.

17. Blackburn, M.J. Trans. Metall. Soc., v. 239, 1967, p. 1200-1208.

18. Kelto, C.A. *Metals Handbook: Powder Metallurgy.* ASM, v. 7, 9th ed., 1990, p. 542-546.

19. Porter, W.J., Osborne, N.R., Eylon, D., and Clifford, J.P. *Advances in Powder Metallurgy.* MPIF Pub., 1990, p. 243-257, and private communication with D. Eylon.

20. Pasternak, R.E., Pepi, M.S., Pelletier, G.P., Amos, C.W., and Valvanis, N.D. *Test Specimen for Mechanical Property Determination.* MTL SP 87-5, p. 9 & 27.

21. Blackburn, M.J., and Smith, M.P. *Improved Toughness Alloys Based on Titanium Aluminides.* Final TR for Period 1985 through March 1989, Wright-Patterson Air Force Base, 1989, p. 87-116.

DISTRIBUTION LIST

No. of Copies	To
1	Office of the Under Secretary of Defense for Research and Engineering, The Pentagon, Washington, DC 20301
	Director, U.S. Army Research Laboratory, 2800 Powder Mill Road, Adelphi, MD 20783-1197
1	ATTN: AMSRL-OP-SD-TP, Technical Publishing Branch
1	AMSRL-OP-SD-TM, Records Management Administrator
	Commander, Defense Technical Information Center, Cameron Station, Building 5, 5010 Duke Street, Alexandria, VA 23304-6145
2	ATTN: DTIC-FDAC
1	MIA/CINDAS, Purdue University, 2595 Yeager Road, West Lafayette, IN 47905
	Commander, Army Research Office, P.O. Box 12211, Research Triangle Park, NC 27709-2211
1	ATTN: Information Processing Office
	Commander, U.S. Army Materiel Command, 5001 Eisenhower Avenue, Alexandria, VA 22333
1	ATTN: AMCSCI
	Commander, U.S. Army Materiel Systems Analysis Activity, Aberdeen Proving Ground, MD 21005
1	ATTN: AMXSY-MP, H. Cohen
	Commander, U.S. Army Missile Command, Redstone Arsenal, AL 35809
1	ATTN: AMSMI-RD-CS-R/Doc
	Commander, U.S. Army Armament, Munitions and Chemical Command, Dover, NJ 07801
2	ATTN: Technical Library
	Commander, U.S. Army Natick Research, Development and Engineering Center, Natick, MA 01760-5010
1	ATTN: Technical Library
	Commander, U.S. Army Satellite Communications Agency, Fort Monmouth, NJ 07703
1	ATTN: Technical Document Center
	Commander, U.S. Army Tank-Automotive Command, Warren, MI 48397-5000
1	ATTN: AMSTA-ZSK
1	AMSTA-TSL, Technical Library
	President, Airborne, Electronics and Special Warfare Board, Fort Bragg, NC 28307
1	ATTN: Library
	Director, U.S. Army Research Laboratory, Weapons Technology, Aberdeen Proving Ground, MD 21005-5066
1	ATTN: AMSRL-WT

No. of Copies	To
	Commander, Dugway Proving Ground, UT 84022
1	ATTN: Technical Library, Technical Information Division
	Commander, U.S. Army Research Laboratory, 2800 Powder Mill Road, Adelphi, MD 20783
1	ATTN: AMSRL-SS
	Director, Benet Weapons Laboratory, LCWSL, USA AMCCOM, Watervliet, NY 12189
1	ATTN: AMSMC-LCB-TL
1	AMSMC-LCB-R
1	AMSMC-LCB-RM
1	AMSMC-LCB-RP
	Commander, U.S. Army Foreign Science and Technology Center, 220 7th Street, N.E., Charlottesville, VA 22901-5396
3	ATTN: AIFRTC, Applied Technologies Branch, Gerald Schlesinger
	Commander, U.S. Army Aeromedical Research Unit, P.O. Box 577, Fort Rucker, AL 36360
1	ATTN: Technical Library
	U.S. Army Aviation Training Library, Fort Rucker, AL 36360
1	ATTN: Building 5906-5907
	Commander, U.S. Army Agency for Aviation Safety, Fort Rucker, AL 36362
1	ATTN: Technical Library
	Commander, Clarke Engineer School Library, 3202 Nebraska Ave., N, Fort Leonard Wood, MO 65473-5000
1	ATTN: Library
	Commander, U.S. Army Engineer Waterways Experiment Station, P.O. Box 631, Vicksburg, MS 39180
1	ATTN: Research Center Library
	Commandant, U.S. Army Quartermaster School, Fort Lee, VA 23801
1	ATTN: Quartermaster School Library
	Naval Research Laboratory, Washington, DC 20375
2	ATTN: Dr. G. R. Yoder - Code 6384
	Chief of Naval Research, Arlington, VA 22217
1	ATTN: Code 471
	Commander, U.S. Air Force Wright Research & Development Center, Wright-Patterson Air Force Base, OH 45433-6523
1	ATTN: WRDC/MLLP, M. Forney, Jr.
1	WRDC/MLBC, Mr. Stanley Schulman
	U.S. Department of Commerce, National Institute of Standards and Technology, Gaithersburg, MD 20899
1	ATTN: Stephen M. Hsu, Chief, Ceramics Division, Institute for Materials Science and Engineering

No. of Copies	To
1	Committee on Marine Structures, Marine Board, National Research Council, 2101 Constitution Avenue, N.W., Washington, DC 20418
1	Materials Sciences Corporation, Suite 250, 500 Office Center Drive, Fort Washington, PA 19034
1	Charles Stark Draper Laboratory, 555 Technology Square, Cambridge, MA 02139
	Wyman-Gordon Company, Worcester, MA 01601
1	ATTN: Technical Library
	General Dynamics, Convair Aerospace Division, P.O. Box 748, Fort Worth, TX 76101
1	ATTN: Mfg. Engineering Technical Library
	Plastics Technical Evaluation Center, PLASTEC, ARDEC, Bldg. 355N, Picatinny Arsenal, NJ 07806-5000
1	ATTN: Harry Pebly
1	Department of the Army, Aerostructures Directorate, MS-266, U.S. Army Aviation R&T Activity - AVSCOM, Langley Research Center, Hampton, VA 23665-5225
1	NASA - Langley Research Center, Hampton, VA 23665-5225
	U.S. Army Vehicle Propulsion Directorate, NASA Lewis Research Center, 2100 Brookpark Road, Cleveland, OH 44135-3191
1	ATTN: AMSRL-VP
	Director, Defense Intelligence Agency, Washington, DC 20340-6053
1	ATTN: ODT-5A (Mr. Frank Jaeger)
	U.S. Army Communications and Electronics Command, Fort Monmouth, NJ 07703
1	ATTN: Technical Library
	U.S. Army Research Laboratory, Electronic Power Sources Directorate, Fort Monmouth, NJ 07703
1	ATTN: Technical Library
	Director, U.S. Army Research Laboratory, Watertown, MA 02172-0001
2	ATTN: AMSRL-OP-WT-IS, Technical Library
10	Authors